Remote Sensing of Environment 278 (2022) 113087

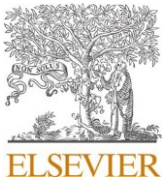

Contents lists available at ScienceDirect

Remote Sensing of Environment

journal homepage: www.elsevier.com/locate/rse

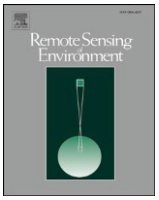

Large loss and rapid recovery of vegetation cover and aboveground biomass over forest areas in Australia during 2019–2020

Yuanwei Qin [a], Xiangming Xiao [a,*], Jean-Pierre Wigneron [b,*], Philippe Ciais [c], Josep G. Canadell [d], Martin Brandt [e], Xiaojun Li [b], Lei Fan [f], Xiaocui Wu [g], Hao Tang [h], Ralph Dubayah [i], Russell Doughty [j], Sean Crowell [k], Bo Zheng [l], Berrien Moore III [k]

[a] Department of Microbiology and Plant Biology, Center for Earth Observation and Modeling, University of Oklahoma, Norman, OK 73019, USA
[b] ISPA, UMR 1391, INRAE Nouvelle-Aquitaine, Bordeaux Villenave d'Ornon, France
[c] Laboratoire des Sciences du Climat et de l'Environnement, LSCE/IPSL, CEA-CNRS-UVSQ, Universit´e Paris-Saclay, 91191 Gif-sur-Yvette, France
[d] CSIRO Oceans and Atmosphere, Canberra, ACT, Australia
[e] Department of Geosciences and Natural Resource Management, University of Copenhagen, Copenhagen, Denmark
[f] Chongqing Jinfo Mountain Karst Ecosystem National Observation and Research Station, School of Geographical Sciences, Southwest University, Chongqing, China
[g] Agroecosystem Sustainability Center, Institute for Sustainability, Energy, and Environment, University of Illinois Urbana-Champaign, Urbana, IL 61801, USA
[h] Department of Geography, National University of Singapore, 1 Arts Link, Kent Ridge 117570, Singapore
[i] Department of Geographical Sciences, University of Maryland, College Park, MD, USA
[j] Division of Geological and Planetary Sciences, California Institute of Technology, Pasadena, CA 91125, USA
[k] College of Atmospheric and Geographic Sciences, University of Oklahoma, Norman, OK 73019, USA
[l] Institute of Environment and Ecology, Tsinghua Shenzhen International Graduate School, Tsinghua University, Shenzhen 518055, China

ARTICLE INFO

Edited by: Jing M. Chen

Keywords:
Forest
Carbon
Remote sensing
Forest recovery
Climate change
Fire

ABSTRACT

Australia experienced multi-year drought and record high temperatures, and massive forest fires occurred across the southeast in 2019 and early 2020. In the fire-affected forest areas, understory and often tree canopies were burned, and in-situ observations in late 2020 reported rapid vegetation recovery, including grasses, shrubs, and tree canopies from burned-but-not-dead eucalyptus trees. Considering the strong fire resilience and resistance of eucalyptus trees and above-average rainfall in 2020, we assessed how much and how quickly vegetation structure and biomass changed from loss to post-fire and drought recovery in 2020 for all forest areas in Australia. Here, we analyzed space-borne optical, thermal, and microwave images to assess changes in the structure and function of vegetation using four vegetation indices (VIs), leaf area index (LAI), solar-induced chlorophyll fluorescence (SIF), gross primary production (GPP), and aboveground biomass (AGB). We found that all eight variables show large losses in 2019, driven by fires and climate (drought and high temperature), but large gains in 2020, resulting from the high resilience of most trees to fire and rapid growth of understory vegetation under wet condition in 2020. In 2019, the forest area has an AGB loss of 0.20 Pg C, which is ~15% of the pre-fire AGB. Attribution analyses showed that both fire and climate (prior and co-occurring severe drought and record high temperatures) are responsible for the AGB loss in 2019, approximately 0.09 Pg C (fire) and 0.11 Pg C (climate), respectively. In 2020, the forest area has a total AGB gain of 0.26 Pg C, composed of 0.22 Pg C from fire-affected forest area and 0.04 Pg C from fire-unaffected forest area. Fire-adapted Eucalyptus forests and above-average annual precipitation in 2020 brought by a moderate La Nin˜a drove the recovery of vegetation cover, productivity, and AGB. The results from this study shows the potential of multiple sensors for monitoring and assessing the impacts of fire and climate on the forest areas in Australia and their post-fire recovery.

1. Introduction

Droughts, heatwaves, and fires could result in large losses of vegetation cover (e.g., leaf area index, LAI), gross and net primary production (GPP, NPP), and aboveground biomass (AGB) (Bowman et al., 2021a; Brandt et al., 2018b; Choat et al., 2012; Ciais et al., 2005;

* Corresponding authors.
E-mail addresses: xiangming.xiao@ou.edu (X. Xiao), jean-pierre.wigneron@inrae.fr (J.-P. Wigneron).

https://doi.org/10.1016/j.rse.2022.113087
Received 27 October 2021; Received in revised form 9 May 2022; Accepted 14 May 2022
Available online 25 May 2022

Hubau et al., 2020; Seidl et al., 2017). In Australia, annual rainfall in 2019 was 275 mm, which was half of the long-term average annual precipitation value, and annual mean air temperature in 2019 was 1.5 °C above the long-term average annual mean air temperature value (the 1961–1990 average). Both were partly driven by the very strong positive phase of the Indian Ocean Dipole (IDO) (King et al., 2020). In addition, fire occurred extensively in 2019, and the spatial extent of forest fires from July 2019 to February 2020 in southeastern Australia was unprecedented in the records starting in the early twentieth century (Canadell et al., 2021). Several studies estimated fire-induced carbon dioxide (CO_2) emission in southeastern Australia using in-situ data, remote sensing, and Earth system models, and these estimates have a large range and uncertainty (Bowman et al., 2021b; DISER, 2020; Li et al., 2021; Sanderson and Fisher, 2020; Shiraishi and Hirata, 2021; van der Velde et al., 2021). Carbon loss estimates from Earth system models were two-thirds lower than those from the Global Fire Emission Database (GFED) (Sanderson and Fisher, 2020). The fire-induced CO_2 emission was about 0.15 Pg C, when satellite-based burned area by the GFED and other satellite datasets were used (Shiraishi and Hirata, 2021). One study estimated that ~0.05 Pg C was released during the 2019/2020 bushfires across eastern and southern Australia using active fire data from the Moderate Resolution Imaging Spectroradiometer (MODIS), Visible Infrared Imaging Radiometer Suite (VIIRS), and Advanced Himawari Imager (AHI) satellite instruments at moderate spatial resolutions and biomass-burning emission inventories (Li et al., 2021). Another study reported a loss from fires of 0.20 Pg C (a range of 0.14–0.24 Pg C) of CO_2 emission from November 2019 to January 2020 based on satellite observations of the TROPOspheric Monitoring Instrument (TROPOMI) carbon monoxide, an analytical Bayesian inversion, and the observed ratios between emitted CO_2 and carbon monoxide (van der Velde et al., 2021). This CO_2 emission estimate is consistent with the estimate from a bottom-up bootstrap approach (0.18 Pg C, a range of 0.08–0.28 Pg C) (Bowman et al., 2021b), but is more than twice the average fire-induced CO_2 emission from five different fire inventories (van der Velde et al., 2021). Another study combined the TROPOMI carbon monoxide and Orbiting Carbon Observatory 2 (OCO-2) CO_2 and reported a similar carbon emission of 0.11–0.24 Pg C (Byrne et al., 2021). The Department of Industry, Science, Energy and Resources in Australia estimated net emissions of 0.23 Pg C during the fire season in 2019–2020 (by February 11, 2020), including 0.26 Pg C absolute emissions and 0.03 Pg C sequestration from vegetation growth and recovery (DISER, 2020).

Several studies have reported the impacts of forest fires on forest areas and canopy (Abram et al., 2021; Boer et al., 2020; Bowman et al., 2020; Canadell et al., 2021; Nolan et al., 2020). Severe drought, record heat, and unprecedented forest fire caused extensive tree mortality in Australia (De Kauwe et al., 2020). Forest canopies were damaged in over 44% of native forests in southeastern Australia and in more than 70% of timber plantations in New South Wales (Bowman et al., 2021a). To date, our knowledge on the loss of vegetation AGB over the forest areas in 2019 in Australia is very limited.

Post-fire vegetation recovery processes and rates in the forest areas

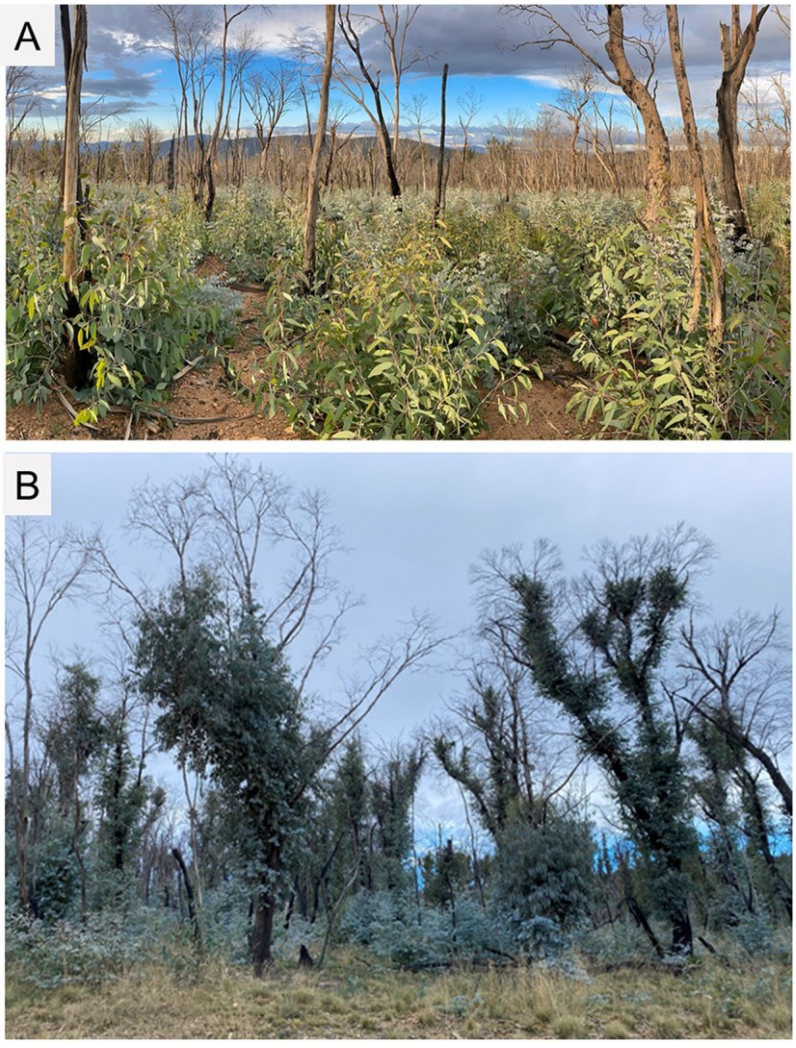

Fig. 1. Field photos of forest recovery (April 2021) after drought and fire (January 2020) in Namadgi National Park, Australia Capital Territory, Australia (Photo: Josep Canadell), showing two key strategies of *eucalyptus* forests to recovery. (**A**) Trees are not dead, but the stem buds were damaged by the fire, and therefore the trunk is effectively unable to recover, i.e., is dead. However, buds at the bottom of the trunk and often part of a lignotuber buried were protected and have been stimulated to grow as there is no longer the top dominance that inhibits their growth. (**B**) Trees were not killed and the thicker bark protected the tissue holding viable buds to resprout. The only components that died were thinner branches at the top of the canopy.

are affected by many factors, including tree survival, climate, and soil nutrients. As shown in the photos from the fields (Fig. 1, Table S1), fires in 2019 resulted in varying severity of damages to trees and understory plants in forests, including removal (burning) of the full canopy in many forests. However, many forest stands had epicormic regrowth from different parts of tree trunks and canopies, in addition to understory shrubs and grassy components. Eucalypt trees (Tribe *Eucalypteae)* in Australia are known to be resilient to drought and fire, with most species able to resprout after fire while others grow from seeds and are subject to weather and climate conditions after disturbances (Bowman et al., 2013; Clarke et al., 2015). Because of the moderate La Nin˜a (Fig. S1), southeastern Australia received above-average annual precipitation and experienced cool temperatures (Figs. S2, S3) in 2020, which could support the recovery of burned-but-not-dead trees and rapid growth of understory plants. One study reported a partial recovery (GPP increase) and greening in un-burned ecosystems but not in the fire-affected areas in the southeast of Australia during February–June 2020, due to cooler conditions and above-average rainfall (Byrne et al., 2021). To date, our knowledge on the recovery of vegetation cover and AGB over the forest area in Australia is very limited, given the vast extension of the area affected in 2019 and 2020. Furthermore, a continental assessment of the recovery of forest areas has not been conducted yet.

In this study, for the first time, we assessed the losses and gains of vegetation cover and AGB in forest areas in Australia due to the concurrent effects of drought, high temperatures and fire using complementary satellite-based indicators. First, we quantified temporal changes in vegetation cover from 2018 to 2020, using vegetation indices (VIs) and LAI (Myneni et al., 2015) from MODIS sensor, solar-induced chlorophyll fluorescence (SIF) data from the TROPOMI instrument (Bacour et al., 2019; Guanter et al., 2015; Kohler et al., 2018), and GPP from the data-driven Vegetation Photosynthesis Model (VPM) (Zhang et al., 2017a). Second, we assessed temporal changes of vegetation AGB, using microwave L-band Vegetation Optical Depth (VOD) observations (Brandt et al., 2018b; Fan et al., 2019; Li et al., 2022; Wigneron et al., 2020), which are linearly related to AGB and show less saturation than other X-band and C-band VOD datasets (Brandt et al., 2018b; Li et al., 2020b; Rodriguez-Fernandez et al., 2018). L-VOD and AGB datasets were evaluated against backscatter data from the Phased Array type L-band Synthetic Aperture Radar onboard the Advanced Land Observing Satellite (ALOS/PALSAR) (Hamdan et al., 2014; Lucas et al., 2010; Shimada et al., 2014), and tree biomass from in-situ plots (Lucas et al., 2010; Paul et al., 2016). Note that L-VOD-based vegetation AGB data over the forest areas include trees, shrubs, and grasses within a grid cell, and for simplicity, in this paper we treat "vegetation AGB" and "forest AGB" interchangeably and use "forest AGB" in the remaining text as our study is focused on forest areas. Third, we performed an attribution analysis to evaluate the relative contribution of fires, high temperatures, and severe drought (rainfall shortage) to the loss of forest AGB in 2019 and to identify the factors affecting the recovery of forest AGB in 2020.

2. Materials and methods

2.1. PALSAR/MODIS forest map

We used the 50-m PALSAR/MODIS forest map in 2010 (Qin et al., 2021), which was generated by using PALSAR Fine Beam Dual Polarization (FBD) data at the 50-m spatial resolution, MODIS/Terra MOD13Q1 data (Vegetation Indices 16-Day L3 Global 250 m) in 2010 and the PALSAR/MODIS forest mapping tool, which has been successfully evaluated in South America (Qin et al., 2019; Qin et al., 2017) and monsoon Asia (Qin et al., 2016; Qin et al., 2015). The PALSAR/MODIS forest map in Australia has been validated by extensive field survey sites, very high spatial resolution images, and LiDAR strip images, and has also been compared with multiple vegetation maps in Australia (Qin et al., 2021). We aggregated the 50-m PALSAR/MODIS forest map into 25-km grid cells, and calculated forest area fractions within the grid cells (Fig. 2A, B). The 2010 map of forest fraction map at 25-km spatial resolution was used to support the analysis of LAI, VIs, GPP, SIF, L-VOD and AGB at 25-km spatial resolution. In Australia, there are 366 forest grid cells with a forest area fraction larger than 30% (Fig. 2C), 216 of which are distributed in southeastern Australia (New South Wales, Victoria, and Australian Capital Territory). In this study, the data analyses were carried out over those 366 forest grid cells, which cover a total land area of 292×10^3 km^2 and a total forest area of 170×10^3 km^2 in 2010, with an average forest area fraction of ~60%.

2.2. MODIS data products

2.2.1. MODIS active fire data

The MOD14A2 active fire product (MODIS/Terra Thermal Anomalies & Fire 8-Day L3 Global 1-km Collection 6) is an 8-day composite containing the maximum value of the individual pixel classes that are in each 1-km grid cell over the 8-day period (Giglio and Justice, 2015). Each MOD14A2 file consists of two layers (a fire mask and associated quality information). We first identified the good-quality observations (nominal and high confidence) of MOD14A2 active fire and then calculated annual active fire frequency during 2010–2020. We aggregated the annual maximum spatial extent of 1-km active fires (Fig. 2D) into 25-km grid cells using arithmetic mean algorithm. Based on the maximum spatial extent of fire fraction within a 25-km grid cell, the 366 forest grid cells were grouped into two categories: (1) 252 forest grid cells with fire (fire area fraction of the land area larger than 1%) and (2) 114 forest grid cells without fire (fire area fraction of the land area less than or equal to 1%).

2.2.2. MODIS land surface temperature (LST) data

The MOD11A2 product (MODIS/Terra Land Surface Temperature/Emissivity 8-Day L3 Global 1-km SIN Grid, Version 6) provides an average 8-day LST at 1-km spatial resolution (Wan et al., 2015), which is calculated as a simple average of all the observations collected within that 8-day period. We used good-quality observations of daytime land surface temperatures during 2010–2020. According to the MOD11A2 product document, we first multiply a coefficient of 0.02 to convert the LST values into LST in the Kelvin unit. Then we subtracted 273.15 from the LST (Kelvin unit) and got the LST values in the Celsius degree. We aggregated the 1-km LST into 25-km grid cells using arithmetic mean algorithm.

2.2.3. MODIS leaf area index (LAI) data

The MCD15A3H product (MODIS/Terra+Aqua Leaf Area Index/FPAR 4-Day L4 Global 500 m SIN Grid; Collection 6) provides a 4-day composite LAI product at 500-m spatial resolution (Myneni et al., 2015). The LAI algorithm chooses the best-quality pixel available from all the acquisitions of Terra and Aqua satellites within each 4-day period. We calculated the average LAI in January by using the good-quality observations (no cloud) in the month. We aggregated the 500-m LAI into 25-km grid cells using arithmetic mean algorithm.

2.2.4. MODIS surface reflectance and vegetation index data

The MOD091A1 product (MODIS Terra Land Surface Reflectance, Global 500 m, V006) produces surface reflectance data in visible, near-infrared, and shortwave infrared at 8-day temporal resolution. We calculated the Normalized Difference Vegetation Index (NDVI) (Tucker, 1979), Near-Infrared Reflectance of vegetation (NIRv) (Badgley et al., 2017), Enhanced Vegetation Index (EVI) (Huete et al., 2002; Huete et al., 1997), and Land Surface Water Index (LSWI) (Xiao et al., 2002; Xiao et al., 2006; Xiao et al., 2005) vegetation indices using the 8-day 500-m MOD09A1 data product in January for each year from 2010 to 2021. We identified the observations covered by clouds, shadows, and snow as bad-quality observations and excluded them from the analysis. We then calculated the average NDVI, NIRv, EVI, and LSWI using only good-quality observations in the month. We aggregated the 500-m

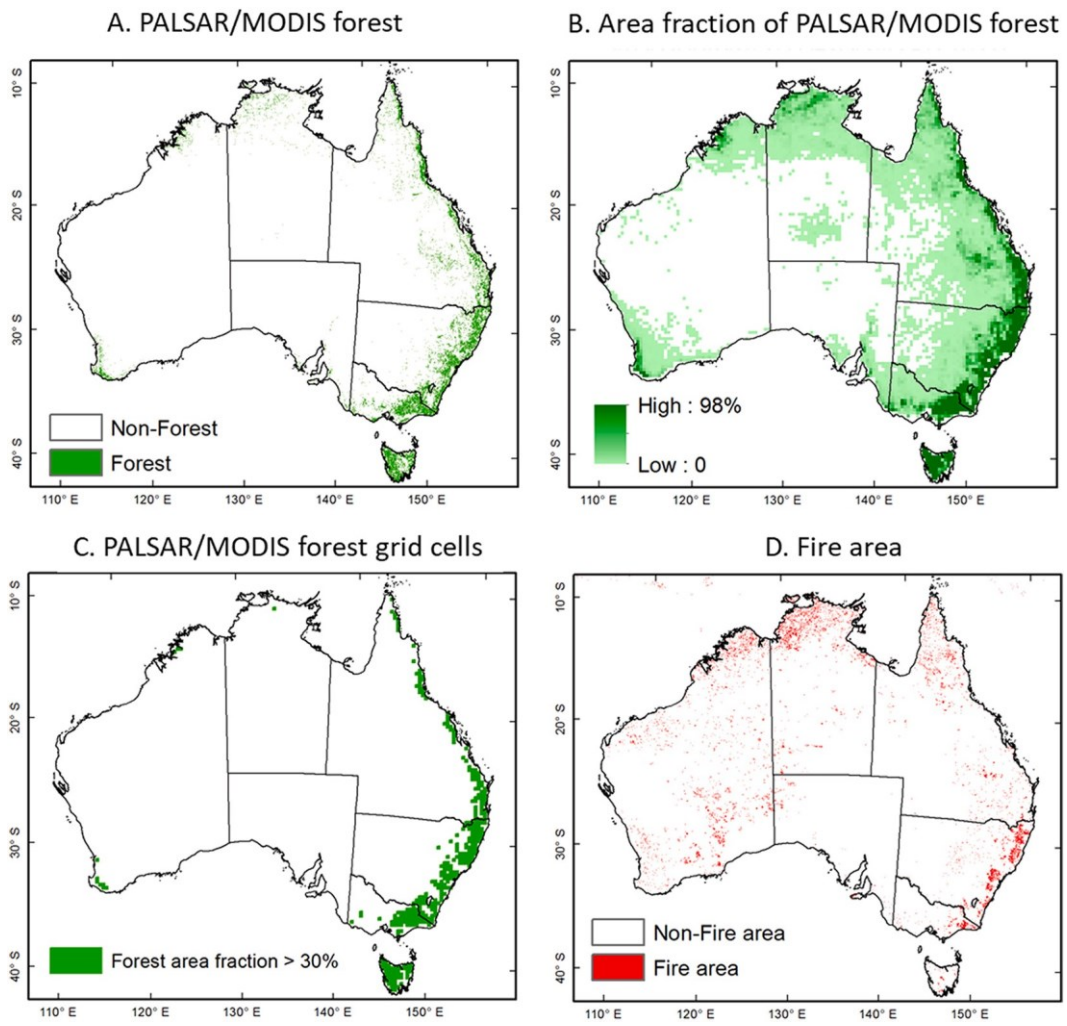

Fig. 2. Spatial distribution of forest and fire in Australia. (**A**) The PALSAR/MODIS forest map at a spatial resolution of 50 m. (**B**) The area fraction of the PALSAR/MODIS forest map at a spatial resolution of 25 km. (**C**) PALSAR/MODIS forest grid cells (366 grid cells) with forest area fraction more than 30%. (**D**) The fire map in 2019 at a spatial resolution of 1 km.

vegetation indices into 25-km grid cells using arithmetic mean algorithm.

2.3. Gross primary production (GPP) data

We used GPP data (g C/m^2/day) from the VPM, which is a light use efficiency model (Xiao et al., 2004a; Xiao et al., 2004b; Zhang et al., 2017b) and uses MODIS 8-day 500-m surface reflectance product (MOD09A1), the land cover product (MCD12A2), and the downward shortwave radiation and air temperature from the NCEP-DOE Reanalysis 2 dataset (Zhang et al., 2017b). We aggregated the GPP data (g C/m^2/day) at-8-day temporal resolution into annual GPP values (g C m^{-2} yr^{-1}) in 2010–2020. The annual GPP data at 500-m spatial resolution were aggregated to 25-km spatial resolution using arithmetic mean algorithm.

2.4. TROPOMI Solar-induced chlorophyll fluorescence (SIF) data

The TROPOMI onboard the Sentinel-5 Precursor satellite provides near-daily SIF data at a spatial resolution of 3.5 × 7 km at nadir from 2018 to 2020 (Kohler et al., 2018). The SIF data are calculated from the TROPOMI near-infrared band 6 (725–775 nm). The instantaneous SIF was converted to a daily average based on a simple approach proposed by (Frankenberg et al., 2011), which accounts for variations in overpass time, length of the day, and solar zenith angle. The TROPOMI SIF provides valuable contributions to understanding vegetation cover (greenness, LAI, photosynthesis) (Doughty et al., 2019; Turner et al., 2020; Yin et al., 2020). We used the gridded (25-km) monthly TROPOMI SIF data that was aggregated from the near-daily TROPOMI SIF data from 2018 to 2020 in Australia.

2.5. Precipitation data

We used the monthly Global Precipitation Measurement (GPM) version 6 dataset, which is provided by NASA Goddard Space Flight Center (Huffman et al., 2019). The Integrated Multi-satellitE Retrievals for GPM (IMERG) is applied to calculate rainfall estimates by combining multiple precipitation data from passive-microwave instruments, precipitation gauge analyses, and other precipitation estimators. The monthly GPM precipitation data is freely available from 2000 to 2020 and has a spatial resolution of 0.1° × 0.1°. We calculated annual precipitation in Australia from 2010 to 2020 and then aggregated the data to 25-km for analysis using arithmetic mean algorithm.

2.6. SMOS-IC SM and L-VOD datasets

The soil moisture (SM) and L-VOD data products were retrieved from the Soil Moisture and Ocean Salinity (SMOS) passive microwave satellite brightness temperatures (TB) by inverting the L-MEB model (L-band

Microwave Emission of the Biosphere) from the multi-angular and dual-polarized SMOS observations (Fernandez-Moran et al., 2017; Li et al., 2020a; Rodriguez-Fernandez et al., 2018; Wigneron et al., 2017b; Wigneron et al., 2021). L-VOD and SM are well decoupled due to a specificity of SMOS multi-angular capability (Tian et al., 2018). The high accuracy of both the L-VOD and SM have been evaluated in several recent studies (Al-Yaari et al., 2019; Bastos et al., 2018; Brandt et al., 2018a; Rodríguez-Ferna´ndez et al., 2018; Tian et al., 2018). The SM and L-VOD datasets have a spatial resolution of 25 km.

2.6.1. Estimation of aboveground live biomass from SMOS L-VOD data

The L-VOD data is sensitive to the total vegetation water content (Tian et al., 2018), with a nearly linear relationship between them (Jackson and Schmugge, 1991; Wigneron et al., 2017a). The AGB calculated from the L-VOD has been used to analyze the spatio-temporal changes of forest and vegetation AGB in the tropic. It is hard to do the direct validation of L-VOD AGB at a spatial resolution of 25-km; thus, the reliability of L-VOD AGB has been assessed indirectly using multiple AGB maps and annual forest cover maps (Brandt et al., 2018b; Fan et al., 2019; Qin et al., 2021b).

Previous works used L-VOD data derived from both ascending and descending observations over the tropic zones (Fan et al., 2019; Wigneron et al., 2020). Note that Australia is an area that is affected very little by noisy microwave interferences at L-band (Fan et al., 2019), and has complete and good quality ascending and descending observations. The ascending observations were acquired at 6 am local time; at that time, the plant xylem refilling process restores the leaf water potential to values close to the root-zone soil water potential, and an equilibrium is reached in the soil–plant–atmosphere continuum (Konings and Gentine, 2017). As L-VOD data from the ascending observations are slightly higher than those from the descending observations, driven by higher vegetation water in the morning, in this study we used L-VOD data from the ascending observations, which helps to reduce the effect of L-VOD diurnal variation on AGB estimates.

Previous works used annual mean or median L-VOD data to estimate AGB (Brandt et al., 2018b; Fan et al., 2019; Wigneron et al., 2020). Note that the L-VOD data are sensitive to leaves, branches, and trunks. Vegetation cover often has large seasonal dynamics of LAI and water content, which affects the seasonal dynamics of L-VOD data (Wigneron et al., 2020). To further reduce the effect of the seasonal changes of L-VOD on AGB estimation, in this study we used the L-VOD data from the summer season, as LAI and moisture content in plants and soils are high

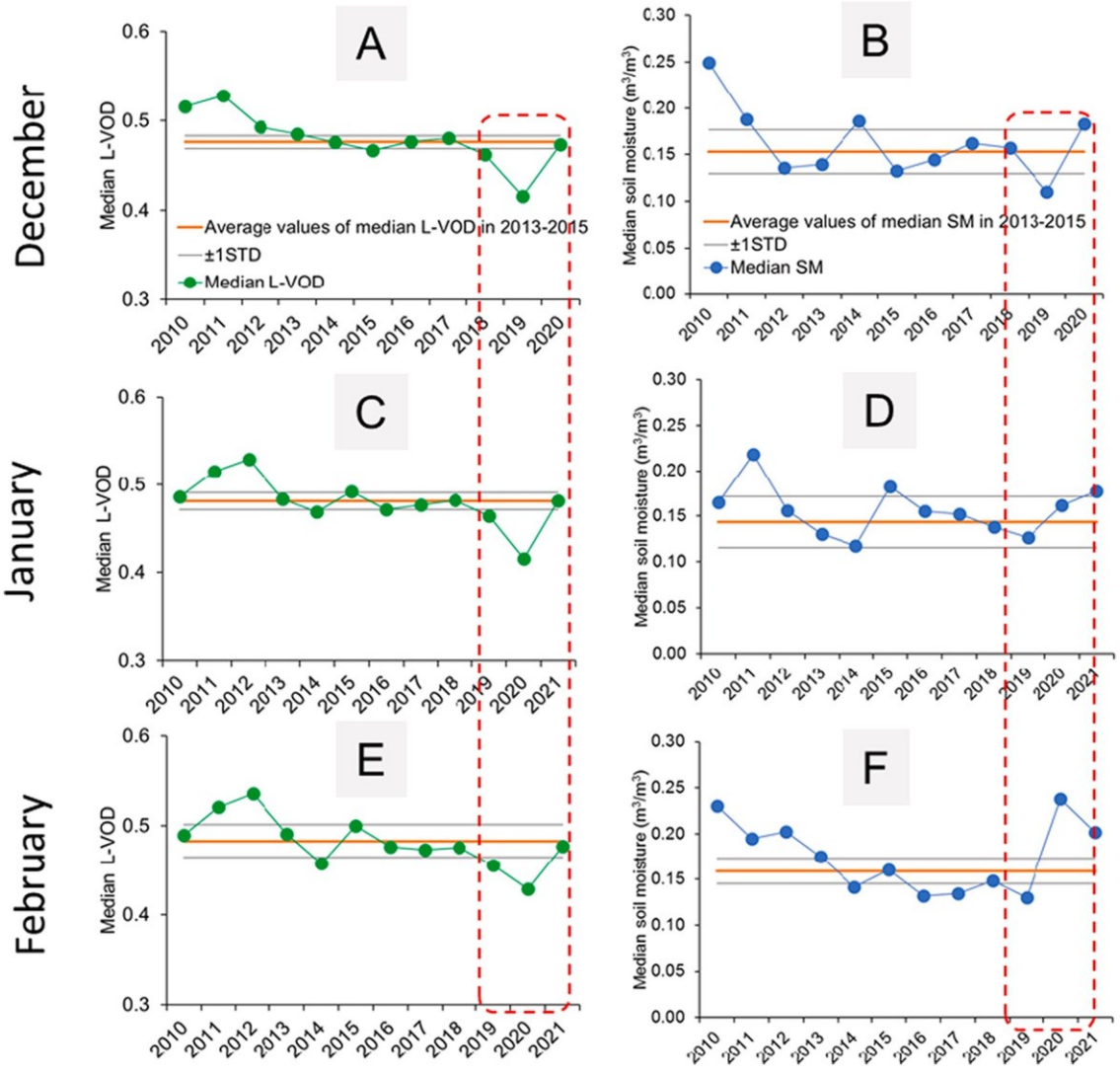

Fig. 3. Monthly median L-VOD and soil moisture in forest grid cells in Australia in summer season (December, January, and February) from 2010 to 2021. (**A, C, E**) Monthly median L-VOD in December, January, and February. The red and gray lines are the average L-VOD and one standard deviation in the reference years (2013–2015). (**B, D, F**) Monthly median soil moisture. The red and gray lines are the average soil moisture and one standard deviation in the reference years (2013–2015). (For interpretation of the references to color in this figure legend, the reader is referred to the web version of this article.)

and usually have relatively small changes over the years under normal climate conditions. In Australia, December–February is hot and wet (Fig. S2B). We compared monthly L-VOD and soil moisture in December, January, and February during 2010–2021 (Fig. 3). Among these three wettest months in a year, soil moisture in January had the least inter-annual variation. In January 2020, the monthly soil moisture anomaly was above-the-average, but the monthly L-VOD anomaly was below-the-average, which indicates the limited effect of water stress on monthly L-VOD in January (Fig. 3). Besides, we quantified the linear relationship between median soil moisture and median L-VOD in December, January, and February from 2010 to 2021 in all forest grid cells in Australia. The median soil moisture and median L-VOD have a significant ($P < 0.05$) linear relationship in December and no significant linear relationship in January ($P = 0.28$) and February ($P = 0.68$) (Fig. S4). As the monthly mean moisture content of vegetation in January has relatively small variation across years, the inter-annual changes of L-VOD in January are mainly driven by AGB change (Frappart et al., 2020). Our study aims to investigate vegetation AGB losses immediately after fires and AGB recovery in a year after fires, thus the use of January L-VOD data to estimate AGB is appropriate. The SMOS L-VOD was converted to carbon density (Mg C ha^{-1}) and then averaged using previously published AGB maps (Avitabile et al., 2016; Baccini et al., 2012; Saatchi et al., 2011) as the references for the regression models between L-VOD and AGB maps (Brandt et al., 2018b; Fan et al., 2019).

2.6.2. Evaluation of L-VOD-based AGB maps

We evaluated L-VOD-based AGB estimates from three perspectives. First, we compared L-VOD with (1) PALSAR data in 2010 at 25-m spatial resolution and (2) two independent AGB datasets in 2015 and 2017. Second, we compared the L-VOD AGB estimate with in-situ inventory plot data. Third, we compared L-VOD AGB estimates calculated from L-VOD in December and January.

PALSAR data: The 25-m L-band PALSAR orthorectified mosaic data product is generated from the observation with minimum response to surface moisture mainly acquired between June and October in each year from 2007 to 2010 and from 2015 to 2020 (Shimada et al., 2014). PALSAR data product has two major data: gamma-naught in HH (horizontal transmitting, horizontal receiving) and HV (horizontal transmitting, vertical receiving), which have been slope corrected and orthorectified. PALSAR HH and HV data have been used to estimate forest AGB in regions (Ma et al., 2017) and the globe (Santoro and Quegan, 2019). Thus, we aggregated the 25-m PALSAR HH and HV in gamma-naught into 25-km grid cells using arithmetic mean algorithm, as indicators of forest AGB, to compare the L-VOD AGB in Australia.

Two independent AGB datasets: We acquired two independent AGB datasets for evaluation. The first AGB dataset was generated and reported by Carreiras et al. (2017b), which is an updated version of the original AGB map generated by Saatchi et al. (2011) corresponding to AGB circa 2015 (Carreiras et al., 2017b). The second AGB dataset was the European Space Agency (ESA) Climate Change Initiative (CCI) AGB dataset, which has a relative error < 20% when AGB is more than 25 Mg C ha^{-1}. The ESA CCI AGB dataset had four epochs (mid-1990s, 2010, 2017, and 2018) at 500-m or 1-km spatial resolution (https://climate.esa.int/en/projects/biomass/). We used the 2017 AGB map. Both the AGB datasets were developed based on optical, lidar and radar satellite images and inventory datasets. In this study, we aggregated (simple averaging method) both the AGB datasets to the 25-km spatial resolution of the SMOS grid using arithmetic mean algorithm (Wigneron et al., 2020).

Biomass data from in-situ inventory plots: The Biomass Plot Library (2022) has collected stem inventory data across Australia since 1936, including over 1 million DBH (diameter at breast height) measurement of ~840,000 trees at ~13,000 sites. Each site has a spatial resolution of 0.05–1 ha. This library has the aboveground, belowground and total biomass (live + dead) estimates calculated using the generic allometric models (Paul et al., 2016) and decay correction factors (Lucas et al., 2010). We downloaded ~9000 sites of AGB data across Australia collected from 2001 to 2015 (Fig. S5) to validate the accuracy and reliability of the L-VOD AGB data in 2010. These ~9000 sites are distributed over 769 L-VOD grid cells. The dry biomass data calculated from in-situ inventory plots (excluding 4 plots with N/A value) and L-VOD AGB have different spatial resolutions (0.05–1.0 ha for in-situ plots vs 25 × 25 km2 for L-VOD grid cells), time periods (2010 vs 2001–2015), and forest definition. To compare the L-VOD AGB with the biomass data from the inventory plots, we first calculated the average AGB (dry mass, Mg ha^{-1}) from those biomass inventory plots within each of 25-km grid cells. Second, we used the forest area fraction map in 2010 to calculate the total and average AGB for each grid cell, which does not include AGB in non-forest area as we have no AGB from the in-situ plots to do such calculation. Finally, we used the 689 grid cells in the 90% confidence range (excluding lower and upper 5% grid cells) to compare the AGB from the inventory plots with the L-VOD AGB (Fig. S5).

2.6.3. Attribution analysis of climate and fire to AGB loss in 2019

First, we estimated the contribution of climate (drought and record high temperatures) and fire to the AGB loss in Australia in 2019 using a linear regression approach (Harris, 2012). The 366 forest grid cells were grouped into two categories: (1) 252 forest grid cells with fire and (2) 114 forest grid cells without fire. The AGB loss for those forest grid cells with fire (252 grid cells) is mainly caused by both climate (drought, record high temperatures) and fire (Eq. 1). The AGB loss for those forest grid cells without fire (114 grid cells) is mainly caused by climate (drought and record high temperatures) only (Eq. 2). Thus, the difference in AGB loss between the two categories can be roughly attributed to fire (Eq. 3).

$$\Delta AGB_{gridcells\ with\ fire} \approx f\left(\Delta AGB_{drought}, \Delta AGB_{temperature}, \Delta AGB_{fire}\right) \quad \text{(Eq. 1)}$$

$$\Delta AGB_{gridcells\ without\ fire} \approx f\left(\Delta AGB_{drought}, \Delta AGB_{temperature}\right) \quad \text{(Eq. 2)}$$

$$\Delta AGB_{fire} \approx \Delta AGB_{gridcells\ with\ fire} - \Delta AGB_{gridcells\ without\ fire} \quad \text{(Eq. 3)}$$

Second, we estimated forest AGB changes (ΔAGB, Tg C) within individual forest grid cells in Australia in 2019 by a simple linear regression model. The independent variables included ΔSM_{mean} (m^3/m^3), ΔLST_{mean} (°C), and their interactions ($\Delta SM_{mean} \times \Delta LST_{mean}$) during October to the following January, and forest fire area (ΔFFA, 10^3 ha) between 2019 and the reference years' average values (2013–2015), as well as AGB (Tg C) in January 2019. Third, we included ΔAGB, ΔSM_{mean}, ΔLST_{mean}, ΔFFA in 2019 and their interactions, and AGB in January 2019 for individual grid cells to build six regression models to estimate forest AGB changes in Australia in 2019. We used the stepwise method and only chose those variables that were statistically significant to build the models, then chose the best model (Eq. 4).

$$\Delta AGB = 5.96\text{–}2.07 \times \Delta LST_{mean} + 47.60 \times \Delta SM_{mean} - 0.04 \times \Delta LST_{mean} \times \Delta FFA + 6.91 \times \Delta SM_{mean} \times \Delta FFA - 2.07 \times \Delta SM_{mean} \times \Delta LST_{mean} \times \Delta FFA - 0.18 \times AGB_{Jan2019} \pm 4.88 \quad \text{(Eq. 4)}$$

3. Results

3.1. Reliability assessment of L-VOD AGB data in Australia

Fig. 4 shows the spatial distributions of L-VOD, L-VOD-based AGB, PALSAR false-color composite (Shimada et al., 2014), and the PALSAR/MODIS forest map (Qin et al., 2021) in 2010 (Fig. 4A-D). L-VOD-based AGB estimates range from < 10 Mg C ha^{-1} to 109 Mg C ha^{-1} in Australia (Fig. 4B), most grid cells with large L-VOD and AGB values occur in the eastern part of Australia and correspond well to large PALSAR HV backscatter coefficient values, an indicator of AGB (Fig. 4C). We investigated the relationships between L-VOD, AGB, PALSAR HV, and the PALSASR/MODIS forest area fraction (FAF) within 25-km grid-cells in 2010 (Fig. 4E, F, H). As the PALSAR data and its threshold value (HV >

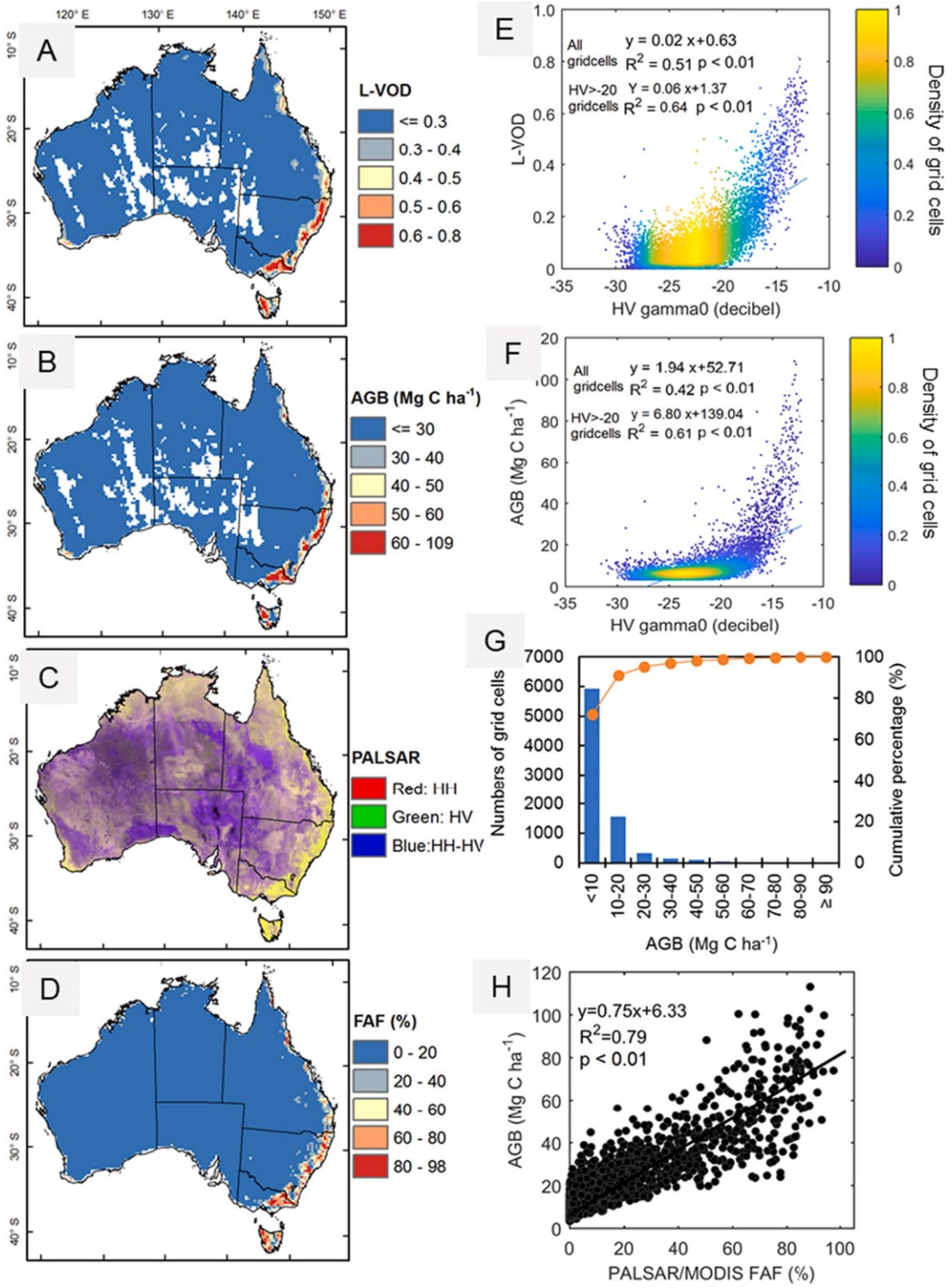

Fig. 4. Spatial distribution of L-VOD, aboveground live biomass (AGB), PALSAR, and PALSAR/MODIS forest area fraction (FAF) maps at a spatial resolution of 25 km in Australia in 2010. (**A**) Spatial distribution of L-VOD. (**B**) Spatial distribution of AGB calculated from L-VOD. (**C**) PALSAR false-color composite map. (**D**) PALSAR/MODIS FAF map. (**E**) Two-Dimension scatter plot between PALSAR HV gamma0 and L-VOD. (**F**) Two-Dimension scatter plot between PALSAR HV gamma0 and AGB. (**G**) Histogram for AGB distribution. (**H**) Two-Dimension scatter plot between PALSAR/MODIS FAF and AGB.

−20) were used to identify and map trees and forests in Australia (Shimada et al., 2014), our regression analyses between PALSAR HV and L-VOD and AGB were conducted for (1) all grid cells and (2) those grid cells with PALSAR HV values of >−20. There are strong linear relationships between L-VOD and PALSAR HV (R^2 = 0.64, P < 0.01), between AGB and PALSAR HV (R^2 = 0.61, P < 0.01) in those grid cells with high backscatter coefficient values (HV > −20; Fig. 4E, F), and between AGB and the PALSAR/MODIS forest area fraction (R^2 = 0.79, P

< 0.01; Fig. 4H).

To assess the sensitivity of L-VOD to AGB estimates in Australia, we also evaluated the relationships between L-VOD and two independent AGB datasets at moderate spatial resolution in Australia. We found that L-VOD had strong non-linear relationships with the AGB estimates in 2015 (Carreiras et al., 2017b; Saatchi et al., 2011) and the AGB estimates in 2017 (Santoro and Quegan, 2019), with L-VOD showing no saturation signal (Fig. S6). The two AGB data sets calculated from L-VOD in December and January were consistent, and their average difference was only 0.01 Pg C during 2011–2021 (Fig. S7), suggesting the L-VOD AGB estimates are little affected by soil moisture.

The L-VOD-based AGB in 2010 also had a strong linear relationship ($R^2 = 0.72$, $P < 0.01$) with the AGB data collected from ~9000 field tree plots for 2001–2015 in Australia (Lucas et al., 2010; Paul et al., 2016), despite their different spatial scales (plot level vs. 25-km grid L-VOD cells) and temporal scales (2001–2015 vs. 2010; Fig. S5).

The results from these comparisons suggest that the SMOS L-VOD-based AGB dataset developed in this study for Australia is a reasonable dataset and can be used to analyze the spatial-temporal changes of AGB in forest grid cells over the years across Australia.

3.2. Loss and recovery of vegetation cover in forest areas

We selected one fire-affected forest grid cell (25 km spatial resolution) to illustrate the temporal changes in the forest canopy during 2018–2020 (Fig. 5A-G). Our study area is dominated by four climate types, including 1) mild/warm summer, cold winter, 2) warm summer, cold winter, 3) warm humid summer, and 4) hot humid summer (Bureau of Meteorology, 2020). The seasonal dynamics of forest LAI, VIs, SIF, GPP and L-VOD in 2018 and 2019 show that they were high in January 2018 and 2019 but low in July 2018 and 2019. After forest fires occurred in July 2019, LAI and VIs dropped sharply by the end of 2019. LAI and VIs recovered rapidly in early 2020, reached pre-fires / pre-drought levels by mid-2020, and kept high values throughout the remaining months of 2020. SIF and GPP were very low in January 2020 and rose substantially in early 2020 but did not reach pre-fires /pre-drought levels. By the end of 2020, SIF and GPP still did not reach the pre-fires / pre-drought levels. The L-VOD also dropped sharply by the end of 2019 and rose substantially in early 2020 but did not reach pre-fires /pre-drought levels.

Temporal changes of the eight satellite indicators for the 366 forest grid cells in Australia (Fig. 5H-K) also show that the LAI, VIs, GPP, and L-VOD reached a minimum in January 2020 and rose rapidly thereafter back to the pre-fires / pre-drought levels. The maximum values of the monthly LAI, VIs, SIF, GPP and L-VOD in all forest grid cells in 2020 were about 95%–103% of those values in 2019. Temporal changes of LAI, VIs, GPP and L-VOD had similar patterns in (1) 252 forest grid cells with fire (Fig. 5L-O) and (2) 114 forest grid cells without fire (Fig. 5P-S). In addition, we also calculated temporal changes of VIs and LAI using the data at the 1-km spatial resolution, and these vegetation indicators at the 1-km spatial resolution had similar temporal changes (Fig. S8). These figures together clearly indicate large losses of forest canopy and understory vegetation in 2019 and rapid and extensive recovery in 2020 over those fire-affected forest areas and fire-unaffected areas in

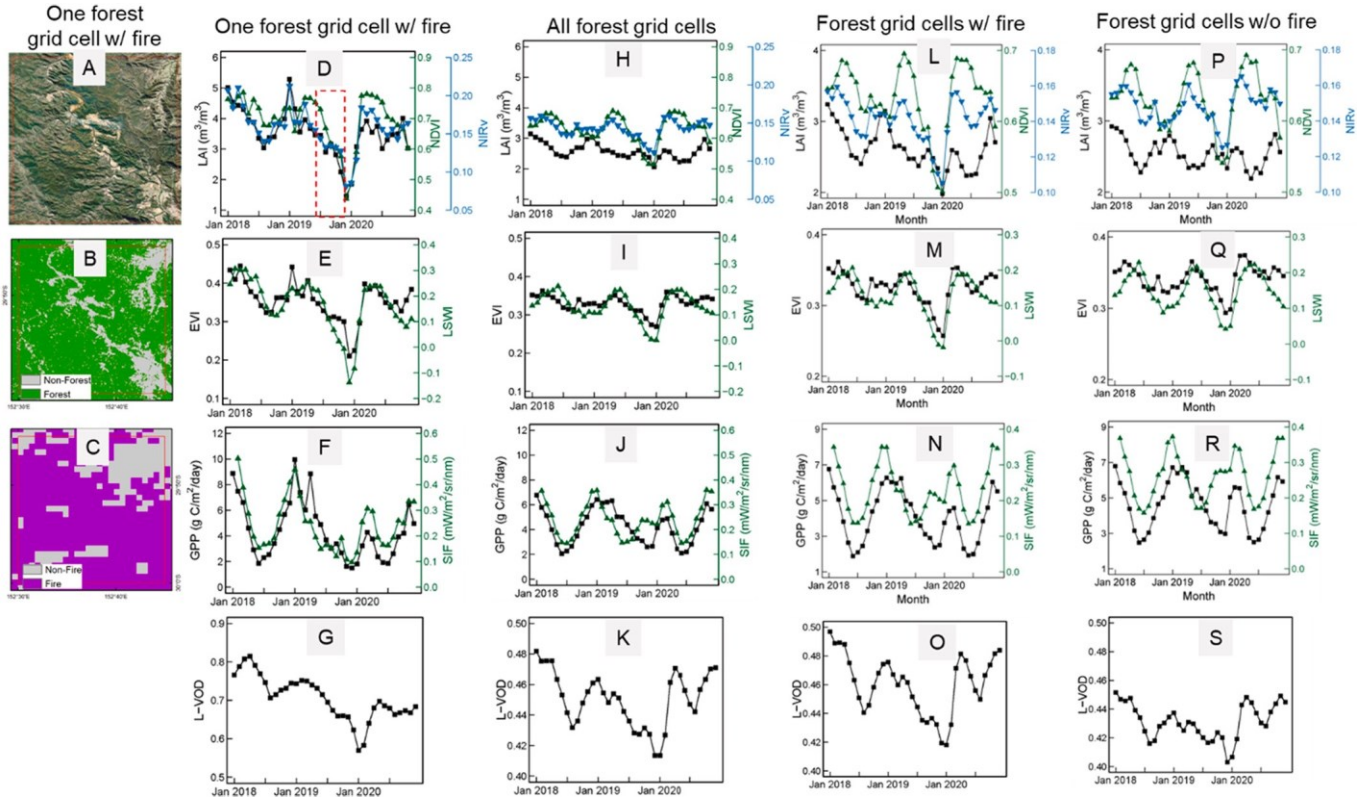

Fig. 5. Monthly average forest leaf area index (LAI), vegetation indices, gross primary production (GPP), solar-induced chlorophyll fluorescence (SIF), and L-band vegetation optical depth (L-VOD) from 2018 to 2020. (**A, B, C**) The natural color composite map, PALSAR/MODIS forest map and fire area map in 2019 in one forest grid cell (center lat / lon: 29.875S / 152.625E) with fire area fraction more than 70%. (**D, E, F, G**) Monthly average LAI, Normalized Difference Vegetation index (NDVI) and Near-Infrared Reflectance of vegetation (NIRv), Enhanced Vegetation Index (EVI) and Land Surface Water Index (LSWI), GPP and SIF, and L-VOD from 2018 to 2020 in the selected forest grid cell shown in (**A, B, C**). The red rectangle in **D** shows the months (from July to November) with fire in 2019. (**H, I, J, K**) Monthly average LAI, NDVI and NIRv, EVI and LSWI, GPP and SIF, and L-VOD from 2018 to 2020 in all forest grid cells. (**L, M, N, O**) Monthly average LAI, NDVI and NIRv, EVI and LSWI, GPP and SIF, and L-VOD from 2018 to 2020 in forest grid cells with fire. (**P, Q, R, S**) Monthly average LAI, NDVI and NIRv, EVI and LSWI, GPP and SIF, and L-VOD from 2018 to 2020 in forest grid cells without fire. (For interpretation of the references to color in this figure legend, the reader is referred to the web version of this article.)

Australia. According to Fig. S2, forest area in Australia had about 400 mm less precipitation in 2019 than the average annual precipitation from 2010 to 2020, especially in the southeast between August and December 2019. The extreme drought and high temperatures suppressed forest growth. Thus, VIs, LAI, GPP, and L-VOD significantly decreased in the forest grid cells without fire with similar or a little smaller magnitude compared to those forest grid cells with fire. This may indicate that 1) the effects of drought on VIs, SIF, GPP and L-VOD were overwhelmingly stronger than the effects of fire, thus both fire-affected and fire-unaffected regions showed a strong drought response. We notice that SIF and GPP had similar seasonal dynamics in 2018, but SIF values did not drop during the fire months of 2019 (Fig. 5J, N, R). The different seasonal changes of VIs, LAI, GPP and SIF may be also attributed to the effect of fire-induced aerosols in the atmosphere on their retrieval and more study on the retrieval of SIF under large fire events is needed in the future.

3.3. Loss and recovery of vegetation AGB in forest areas

Annual AGB summed over the 366 forest grid cells during 2010–2021 (Fig. 6) varied from 1.59 Pg C in January 2012 to 1.10 Pg C in January 2020 (Fig. 6A). The average total AGB over the three reference years (2013–2015, with similar annual precipitation) was 1.37 Pg C (a carbon density of 46.93 Mg C ha^{-1}). These 366 forest grid cells had a net loss of 0.20 Pg C (6.71 Mg C ha^{-1}) AGB between January 2019 and January 2020 (~15% of 1.37 Pg C AGB; Fig. 6B). The AGB in the 252 forest grid cells with fire decreased from 0.93 Pg C (45.9 Mg C ha^{-1}) in January 2019 to 0.76 Pg C (37.8 Mg C ha^{-1}) in January 2020 (Fig. 6A), an AGB loss of 0.17 Pg C (Fig. 6B), accounting for 85% of the 0.20 Pg C loss. The AGB in the 114 forest grid cells without fire decreased from 0.37 Pg C (40.5 Mg C ha^{-1}) in January 2019 to 0.34 Pg C (36.9 Mg C ha^{-1}) in January 2020 (Fig. 6A), an AGB loss of 0.03 Pg C (Fig. 6B), accounting for 15% of the 0.20 Pg C loss. We further investigated the relative contributions of climate and fire on the AGB loss in January 2019 – January 2020 over the 366 forest grid cells in Australia (Eq. 1–3). We calculated the average AGB change (−3.65 Mg C/ha) from all the 114 grid cells without fire and the average AGB change (−8.10 Mg C/ha) from all the 252 grid cells with fire. Then we calculated the difference (−4.46 Mg C/ha) in average AGB changes as the climate-induced AGB change in the 252 grid cells with fire. The contribution from climate (0.11 Pg C) is slightly higher than from fire (0.09 Pg C), suggesting the severe impacts of both record high temperatures and drought on forest AGB dynamics.

We quantified the sensitivity of forest AGB change to forest fire area, soil moisture, and land surface temperature at grid-cell scale (Fig. 7). As climate variables have large interannual variations, we used the averaged values in 2013–2015 as the references and calculated anomalies (differences; *Methods*). Forest AGB change over the 366 forest grid cells had significant but moderately strong linear relationships with forest fire area (R^2 = 0.44, P < 0.01) and land surface temperature (R^2 = 0.46, P < 0.01), and no strong linear relationship with soil moisture (R^2 = 0.09, P < 0.01) changes (Fig. 7A-C). In the 252 forest grid cells with fire, AGB changes had significant linear relationships with fire area (R^2 = 0.41, P < 0.01) and land surface temperature (R^2 = 0.47, P < 0.01) changes (Fig. 7D-F), suggesting fire and climate together contributed to these AGB losses. In the 114 forest grid cells without fire, AGB changes had significant linear relationships with land surface temperature (R^2 = 0.67, P < 0.01) and soil moisture (R^2 = 0.45, P < 0.01) changes (Fig. 7G-I), suggesting hot temperature and drought were the major contributors to these AGB losses. We developed a multi-variate linear regression

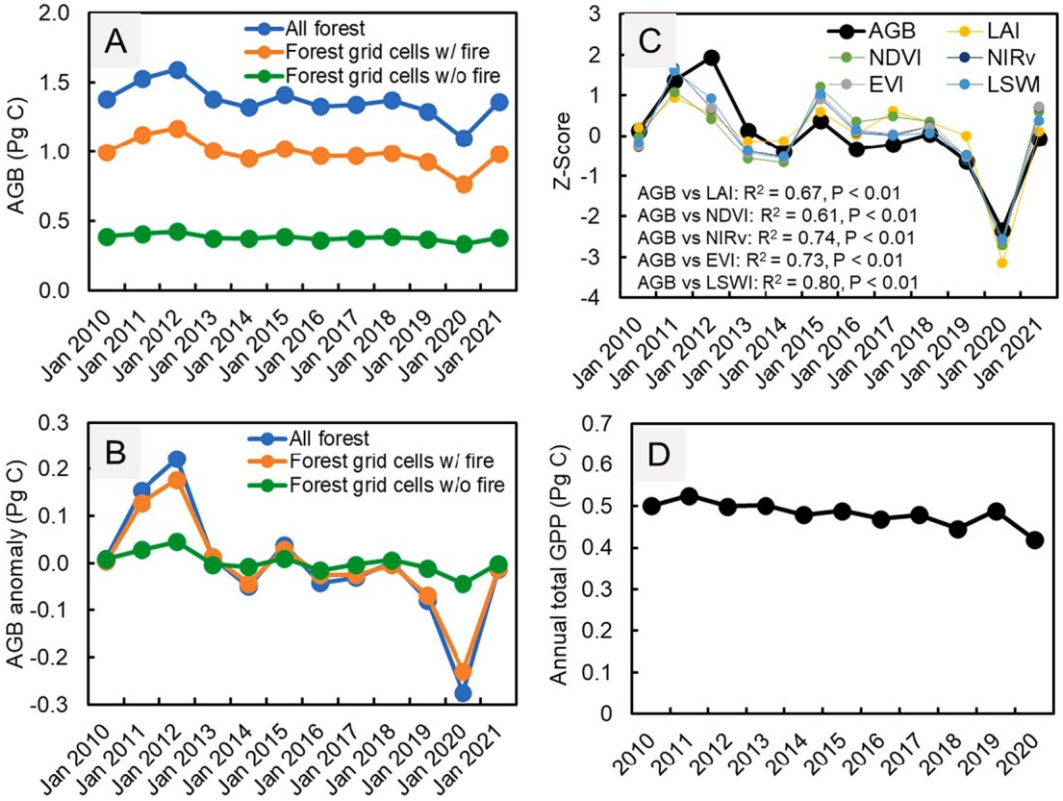

Fig. 6. Interannual changes of forest aboveground biomass (AGB), leaf area index (LAI), vegetation indices, and gross primary production (GPP) in Australia from 2010 to 2021. (**A**) Total AGB in all forest grid cells, forest grid cells with fire, and forest grid cells without fire. (**B**) AGB anomaly in all forest grid cells, forest grid cells with fire, and forest grid cells without fire. (**C**) *Z*-Score values of forest AGB and vegetation indices and their linear relationships. (**D**) Annual total GPP in all forest grid cells. Vegetation indices include Normalized Difference Vegetation index (NDVI), Near-Infrared Reflectance of vegetation (NIRv), Enhanced Vegetation Index (EVI) and Land Surface Water Index (LSWI).

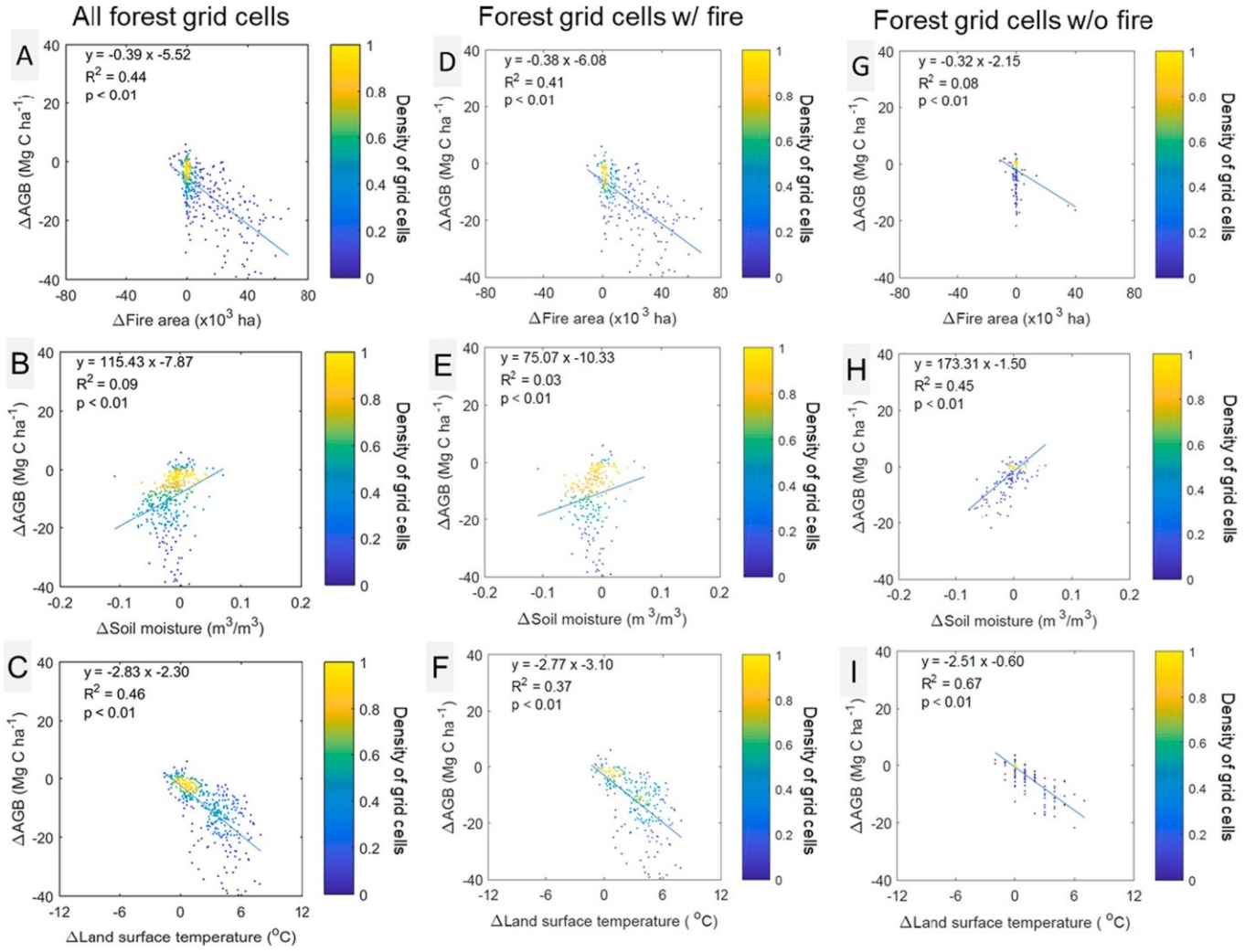

Fig. 7. Two-dimension scatter plots between aboveground biomass (AGB) changes and fire area, soil moisture (SM), and land surface temperature (LST) changes in forest in Australia in 2019. (**A, B, C**) Two-Dimension scatter plots between ΔAGB and ΔFire area, ΔSM, and ΔLST in all forest grid cells. (**D, E, F**) Two-Dimension scatter plots between ΔAGB and ΔFire area, ΔSM, and ΔLST in forest grid cells with fire. (**G, H, I**) Two-Dimension scatter plots between ΔAGB and ΔFire area, ΔSM, and ΔLST in forest grid cells without fire. ΔAGB are the differences between AGB in January 2020 and the average AGB in reference years (January 2013, January 2014, January 2015). ΔFire area are between fire area in 2019 and average fire area in reference years (2013–2015). ΔSM and ΔLST are the differences between the average $SM_{OCT\text{-}JAN}$ in 2019 and the average $SM_{OCT\text{-}JAN}$ in reference years (2013–2015) and between the average $LST_{OCT\text{-}JAN}$ in 2019 and the average $LST_{OCT\text{-}JAN}$ in reference years (2013–2015).

model (*Methods*) to estimate peak AGB changes in 2019 within each forest grid cell, using anomalies of lagged soil moisture and land surface temperature between October 2019 and January 2020, and forest fire area in 2019 (anomalies relative to average values during 2013–2015), as well as AGB in 2018. This model accounted for 72% of the variance of AGB changes in 2019 in the 366 forest grid cells ($R^2 = 0.72$, $P < 0.01$) at 95% confidence interval. These analyses indicated the compound effects of fire and climate on forest AGB changes in Australia.

By January 2021, annual AGB from the 366 forest grid cells recovered to 1.36 Pg C, reaching a higher value than in January 2019 (1.29 Pg C) and close to the average annual AGB (1.37 Pg C) in 2013–2015 (Fig. 6A). The 366 forest grid cells had an AGB gain of 0.26 Pg C (9.0 Mg C ha^{-1}) between January 2020 and January 2021, contributed by 0.22 Pg C from the 252 forest grid cells with fire and 0.04 Pg C from the 114 forest grid cells without fire (Fig. 6B). As measured by the *Z*-Score values, the interannual variation of AGB in the 366 forest grid cells agreed well with LAI and four VIs over the period of January 2010 to January 2021, and LAI, VIs, and AGB had a large drop by January 2020 and a strong recovery by January 2021 (Fig. 6C). The linear regression analyses showed strong temporal consistency between AGB and VIs, with statistically significant ($p < 0.01$) R^2 values ranging from 0.61 for the NDVI to 0.80 for LSWI. Geographically, the spatial distributions of the difference maps (data in January 2020 minus data in January 2019) and the difference maps (data in January 2021 minus data in January 2020;Fig. 8) showed large losses in LAI, EVI, and SIF in 2019 and large gains in LAI, EVI, and SIF in 2020, consistent with the spatial distribution of AGB change. We grouped the 366 forest grid cells by the changes of annual precipitation and LAI between 2019 and 2020 and forest fire area fraction in 2019 (Fig. 9). LAI (recovery) and AGB (recovery) increased as annual precipitation and forest fire area fraction increased (Fig. 9A-D). AGB (recovery) also increased as LAI (recovery) and EVI (recovery) increased (Fig. 9E, F). These results indicate that the recovery of vegetation cover in 2020 contributes most to the recovery of AGB.

4. Discussion

4.1. Estimation of vegetation AGB in forest areas

Several studies have developed forest AGB maps for the nominal year 2005 over the tropical regions (Baccini et al., 2012; Saatchi et al., 2011),

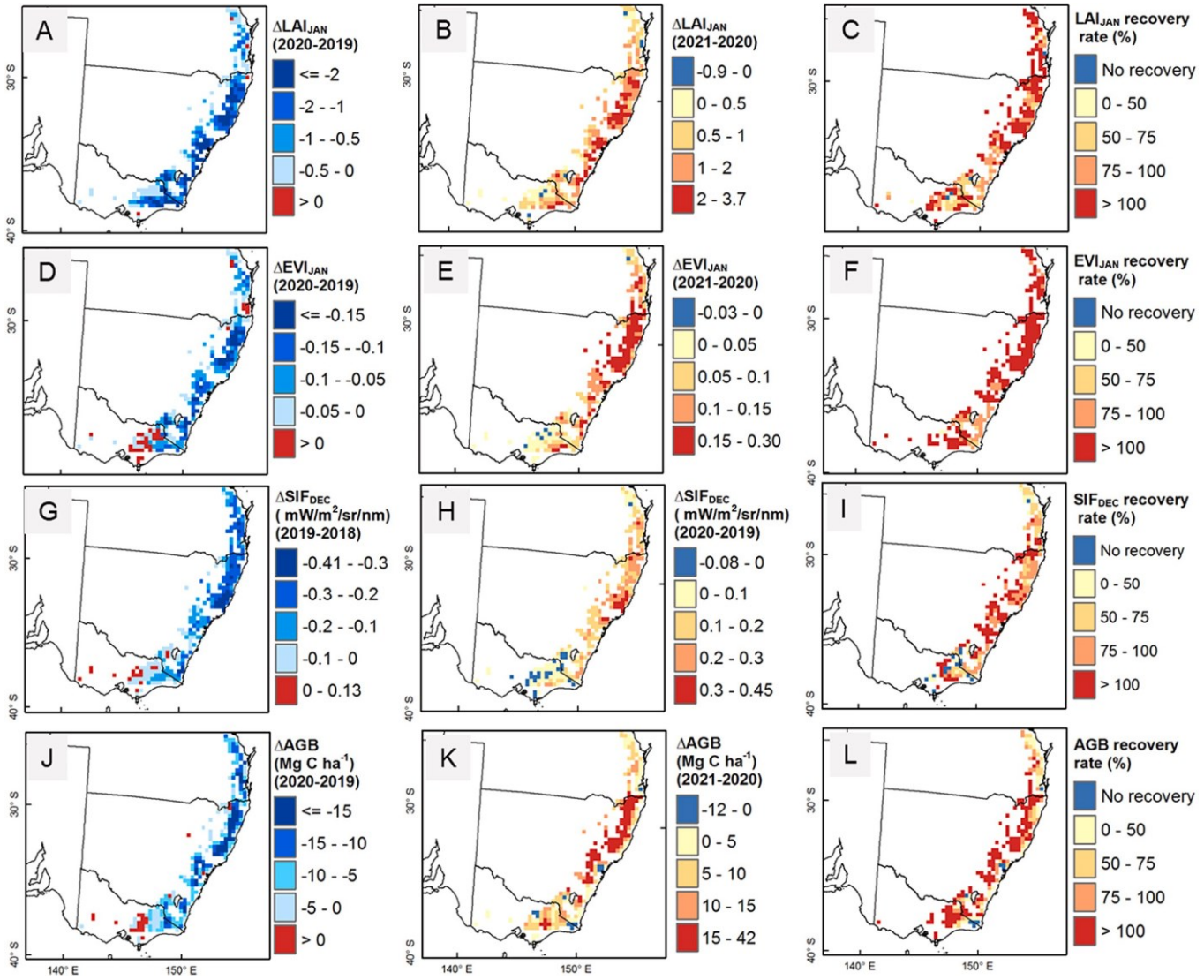

Fig. 8. Spatial distribution of leaf area index (LAI), Enhanced Vegetation Index (EVI), solar-induced chlorophyll fluorescence (SIF), and aboveground live biomass (AGB) changes in southeastern Australia. (**A, D, G, J**) LAI, EVI, SIF, and AGB changes between 2019 and 2020. (**B, E, H, K**) LAI, EVI, SIF, and AGB changes between 2020 and 2021. (**C, F, I, L**) LAI, EVI, SIF, and AGB recovery rate, equal to the ratio between LAI, EVI, SIF, and AGB changes in 2020–2021 and those changes in 2019–2020, respectively.

and the globe (Carreiras et al., 2017b), and reported interannual changes in tropical forest AGB during 2003–2014 (Baccini et al., 2017) and global forest AGB during 2001–2019 (Harris et al., 2021; Xu et al., 2021). These forest AGB maps were generated by using optical satellite images, biomass data calibrated from the Geoscience Laser Altimeter System (GLAS) Lidar footprints, and field data, and the use of these AGB datasets for assessing interannual changes of forest AGB has been in debate (Hansen et al., 2019) as optical image data are largely related to the changes of leaves in the forest canopies and cannot reflect the changes of branches and trunks.

In recent years, daily VOD datasets at coarse spatial resolution, related to the water content of vegetation, were retrieved from image data acquired by multiple passive microwave sensors, offering the potential to track the spatio-temporal changes of vegetation AGB. The VOD data retrieved from the Special Sensor Microwave Imager (SSM/I, Ku-band, 18.70 GHz), Microwave Imager onboard the Tropical Rainfall Measuring Mission (TRMM) (TMI, X-band, 10.65 GHz), and the Advanced Microwave Scanning Radiometer (AMSR-E, C-band, 6.93 GHz; X-band, 10.65 GHz) was used to calculate annual AGB data from 1993 to 2012 and their changes in the globe (Liu et al., 2011; Liu et al., 2015) based on the relationship between VOD and AGB map generated by Saatchi et al. (2011). However, the C−/X−/Ku−band VOD data sets are easy to become saturated in the forest area with high AGB density (Brandt et al., 2018b).

In this study, we improved our understanding of the potential of L-VOD data to estimate forest AGB. First, we used an improved forest cover map (PALSAR/MODIS forest) in Australia (Qin et al., 2021) as a baseline map to select and delineate the appropriate study area to estimate forest AGB losses and gains. Compared with the canopy height and canopy coverage data derived from GLAS LiDAR footprints, the PALSAR/MODIS forest map has 73% of forest pixels meeting the Food and Agriculture Organization (FAO) forest definition, much higher than four widely used forest maps (ranging from 36% to 52%). Second, we investigated the potential of using monthly L-VOD data to quantify the interannual changes in forest AGB. We used the recently developed daily L-VOD data to calculate AGB based on the relationship between L-VOD and ten AGB maps (Fan et al., 2019). The L-VOD AGB, with no obvious saturation to high AGB density (Brandt et al., 2018b; Wigneron et al., 2020), has proven to provide reasonably accurate estimates of forest AGB and its interannual changes since 2010 (Brandt et al., 2018b; Fan

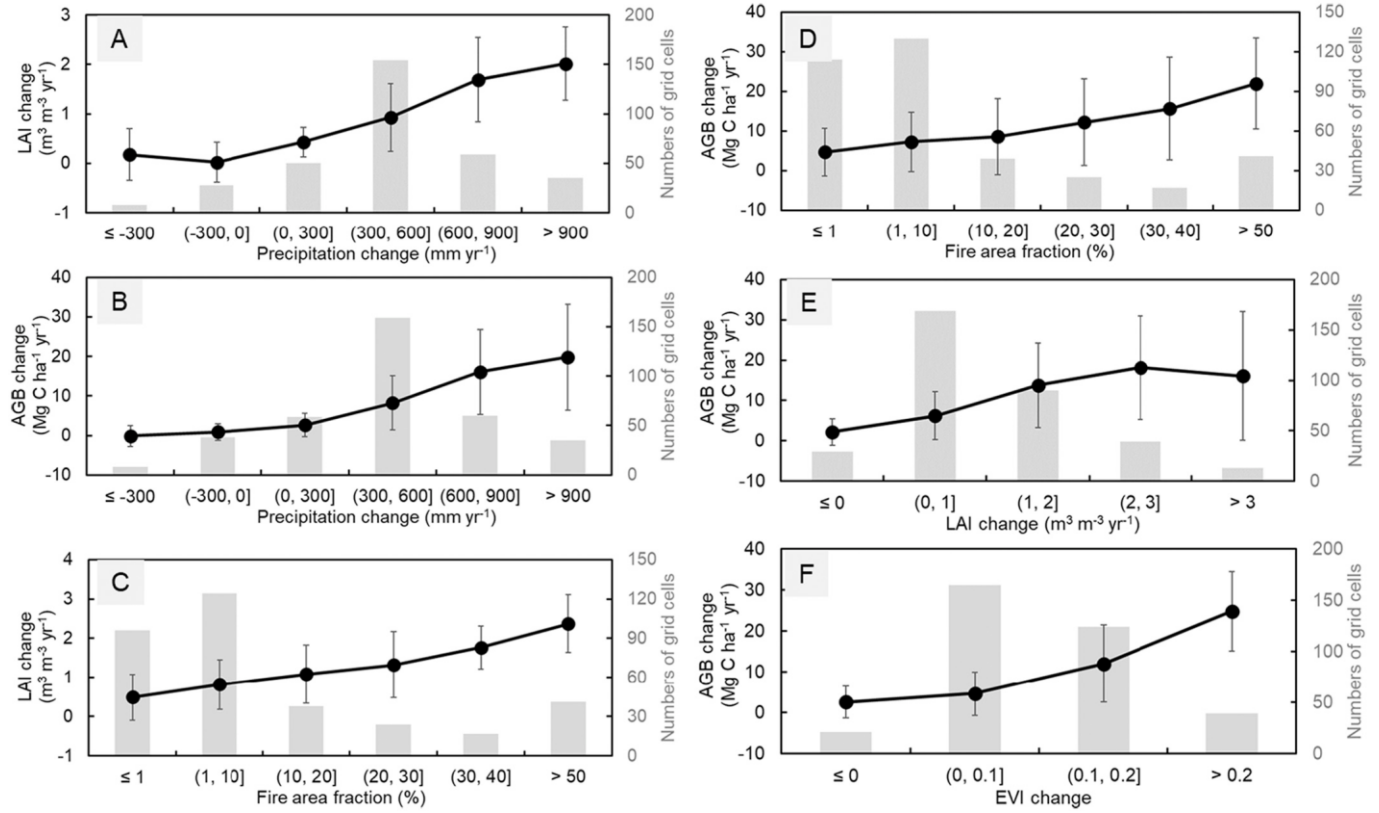

Fig. 9. Forest recovery in Australia between 2019 and 2020. (**A, B**) Leaf area index (LAI) and aboveground biomass (AGB) changes under precipitation change between 2019 and 2020. (**C, D**) LAI and AGB changes between 2019 and 2020 in different fire area intervals in 2019. (**E**) AGB changes in different LAI change intervals between 2019 and 2020. (**F**) AGB change in different Enhanced Vegetation Index (EVI) change intervals between 2019 and 2020. The one standard deviation values were added into the curves. The gray bar graphs are the numbers of grid cells.

et al., 2019; Fernandez-Moran et al., 2017; Qin et al., 2021b; Rodriguez-Fernandez et al., 2018). This study is the first application that uses monthly L-VOD data to estimate the losses and gains of forest AGB in Australia.

Interannual changes of forest AGB is one of the major indicators tracking changes in terrestrial carbon sinks and sources. One study (Harris et al., 2021) estimated forest AGB change between 2001 and 2019 and reported large AGB gains over the forests in southeastern Australia. Our results do not show such large AGB gains during 2010–2019, as forest AGB in January 2019 was similar to the other years (2013–2018) over the 366 forest grid cells (Fig. 6A, B). Over the entire period of January 2010 – January 2021, the net change of total AGB in the 366 forest grid cells was found to be neutral (Fig. 6B). The discrepancy between our study and Harris et al. study can be attributed in part to (1) Harris et al. study focused on forest cover loss, removal by harvest, and forest regrowth and (2) the higher temporal resolution of SMOS L-VOD and AGB datasets used in our study. The use of monthly L-VOD data to estimate forest AGB opens an opportunity for us to develop timely and consistent data of AGB losses and gains under severe drought, heatwave, and extensive fires and then use the resultant data to support and improve the study of the terrestrial carbon cycle

4.2. Vegetation cover and AGB losses in forest areas

The dominant tree species in the forests of the southeast of Australia are capable of resprouting after disturbances. These eucalyptus trees have many special fire-adaptive traits, and most species and individuals are not killed by high severity fire (Crisp et al., 2011). According to field inventories of forest biomass loss caused by fire in the southeast of Australia, the main components leading to biomass loss are small branches (7.6–15.0 Mg C/ha) and leaves and grassy components (3.5–7.0 Mg C/ha) (Keith et al., 2014). Optical remote sensing data mainly capture the changes of upper canopies of forest. Passive microwave remote sensing data (L-VOD) capture the changes of trees (canopy, tree branches and trunks) and understory (grass and shrub). Thus, vegetation indicators calculated from optical and microwave data need to be used together to quantify the temporal changes in the forest canopy and AGB before- and after fire.

A recent study (De Kauwe et al., 2020) reported that more significant tree mortality occurred from 2017 to 2019 than the Millennium drought from 2000 to 2009 in the southeast of Australia. Another recent study (Bowman et al., 2021a) reported that the unprecedented forest fire damaged or reduced forest canopies in over 44% of native forests in southeastern Australia and in more than 70% of timber plantations in New South Wales. Both drought and fire caused significant AGB losses, respectively, as shown in this study. The effects of climate and fire on forest AGB are not independent. Anomalous climate conditions can precondition for fire events and/or exacerbate the impacts of fire. We recognize that it is challenging to accurately estimate the relative contributions of drought or fire to forest AGB losses, as the geospatial dataset we used in this study are at coarse spatial resolution. The in-situ, on-the-ground monitoring of forest AGB changes and high spatial resolution forest AGB datasets are needed to better understand the interactions between climate and fire and quantify the relative roles of individual driving factors for the changes of forest AGB.

4.3. Vegetation cover and AGB gains in forest areas

The rates and paths of vegetation recovery in forest areas after fires, droughts, and heatwaves have been extensively studied (Fu et al., 2017; Schwalm et al., 2017). Many previous studies reported that these disturbances usually have long-term legacy impacts on forest AGB, and

forest AGB recovery was slow and took many years (Wigneron et al., 2020; Yang et al., 2018). The Eucalypt tribe dominates in Australian forests and is adapted to fire and drought. The spatial extent of the 2019 fires made this an exceptionally destructive year. The eucalypt forest AGB loss caused by fires was relatively moderate at the forest stand scale, according to the field assessment in southeastern Australia (DISER, 2020; Keith et al., 2014). One earlier study reported that the forest biomass components combusted by fires in 2009 included dead standing trees (3.8–21.7 Mg C ha^{-1}), small branches (7.6–15.0 Mg C ha^{-1}), litter (6–9 Mg C ha^{-1}), and canopy leaves (3.5–7 Mg C ha^{-1}), dependent upon the fire severity and forest ages in southeastern Australia (Keith et al., 2014). According to the forest fire and recovery report from the Australian Department of Industry, Science, Energy, and Resources (DISER, 2020), bushfires in Australia have substantial impacts on woody debris and understory vegetation, moderate impacts on the upper forest canopy, and small to rare impacts on tree mortality, so that forest cover and AGB can fully recover within 10–15 years at the site level, as it was the case for the 2002/2003 and 2009 bushfires in southeastern Australia. Our study analyzed the changes of forest carbon in the aboveground live biomass for all the forest areas in Australia, which include both fire-affected areas (20%) and fire-unaffected areas (80%) at the spatial resolution of 1 km. Forest growth in the fire-affected areas and fire-unaffected areas supported the rapid AGB recovery in 2020 with the above-the-average rainfall.

The record high temperatures, drought, and unprecedented forest fires in July 2019–February 2020 did remove a significant amount of woody debris, understory vegetation, and upper forest canopy (Fig. 1), but most eucalypt trees were not killed (DISER, 2020). In eucalypt trees, the buds of the sprouts in trunks are often protected by thick bark. Tree canopy has hormones that suppress bud sprouting. After fire removes tree canopy, the hormone-based suppressing of sprouts is also removed, and then bud sprouting could occur, and tree becomes alive again under favorable climate and soil conditions (Crisp et al., 2011). A moderate La Nin˜a event prevailed in 2020, and at the national scale, annual precipitation in 2020 was close to the long-term average (483 mm) and double of annual precipitation in 2019 (Figs. S2, S3). For southeastern Australia, annual precipitation in 2020 (1160 mm) was more than double of 550 mm in 2019 and was above the long-term average of 977 mm during 2010–2020 (Figs. S2, S3). The above-average precipitation in 2020 (both early months and the entire year) could support the strong growth of forest and other understory vegetation components (grass and shrub) in March–April and August–December, as shown by MODIS LAI and VIs, TROPOMI SIF, GPP, and L-VOD (Fig. 5) and the field photos from the citizen science community across Australia (Table S1). The time series NIRv, GPP, and SIF datasets in Byrne's study also showed the unburned and burned forest areas were partially recovered or in the process of recovering before June 2020 (Byrne et al., 2021). The different recovery status in the burned forest areas between this study and Byrne's study may be caused by the differences in study periods, definition of burned areas, and input datasets (Table S2). AGB recovery in 2020 is likely contributed by the extensive forest and understory regrowth both from resprouting and seeding (Bowman et al., 2013; Clarke et al., 2015). Annual GPP (0.42 Pg C/yr) in 2020 for the 366 forest grid cells is close to the multi-year average annual GPP (Fig. 6D). The ratio between NPP and GPP (NPP/GPP, or carbon use efficiency) of *Eucalyptus saligana (Sm.)* forest varies with stand age slightly, ranging from 0.66 at age two years to 0.62 at age six years (Collalti and Prentice, 2019; Ryan et al., 2004). When the NPP/GPP ratio of 0.66 is used, an annual GPP of 0.42 Pg C in 2020 could result in an annual NPP of 0.28 Pg C in 2020, which is slightly higher than forest AGB gain estimate (0.26 Pg C) in 2020. The large forest AGB gain per unit area (~9.0 Mg C ha^{-1} yr^{-1}) in 2020 is within the range of NPP estimates from the established forest (5–18 Mg C ha^{-1} yr^{-1}) (Haverd et al., 2013a; Haverd et al., 2013b; Keith et al., 2010; Roxburgh et al., 2004) and the regenerated forests (9–36 Mg C ha^{-1} yr^{-1}) (Attiwill, 1992; Volkova et al., 2018) in southeastern Australia based on field observations and regional modeling (Table S3). Some of the Australian eucalypt forests have one of the largest AGB per unit land area in the world (Keith et al., 2009). The rapid and large recovery of AGB in 2020 was largely driven by vegetation cover (Fig. 9E, F).

4.4. Challenges and potential solutions for monitoring vegetation cover and AGB

Through remote sensing technology, the changes in vegetation cover and AGB can be monitored with a variety of data products, including SMOS L-VOD and AGB, VIs, LAI, SIF, and GPP, in addition to soil (e.g., soil moisture), atmosphere (e.g., temperature, precipitation) and surface disturbance (e.g., fire extent, forest cover loss). These datasets could be used together to produce a full story of the impacts of climate, fire, and anthropogenic activities on vegetation at any time and any location on the Earth. The L-VOD data have a coarse spatial resolution of 25-km, and thus they cannot be used to assess the forest canopy and AGB changes (loss and recovery) at the site and landscape scales. In this study we demonstrate the potential of monthly L-VOD data for quantifying forest AGB changes at the regional and country scales at coarse spatial resolution. The monitoring and assessment capacity of forest canopy and AGB has been continuously improved with current and new Earth observation missions, for instance, vegetation height and profile data from the Global Ecosystem Dynamics Investigation (GEDI) mission (Dubayah et al., 2020), and high-resolution AGB data from the soon-to-be-launched Biomass mission (Carreiras et al., 2017a). The P-band Biomass satellite, developed by the European Space Agency, is planned to launch in 2023. The P-band with a wavelength of 70 cm, has a longer band wavelength than the L-band (23.5 cm). The Biomass satellite will also provide carbon stock at a much finer spatial resolution in the order of 4 ha, which will help analyze carbon stock changes and the mechanisms at both site and landscape scales. In addition to the above-mentioned satellite data, it is also important to note that more and continuous effort is urgently needed for in-situ and on-the-ground monitoring of post-fire recovery in forests, which could provide rich data to calibrate, validate, and improve the methodology used in this study.

5. Conclusion

Our satellite-based analysis reveals a large loss of forest AGB in 2019, driven by both extreme climate and fires in Australia and the rapid recovery of forest AGB in 2020. The vegetation AGB loss in 2019 and gain in 2020 are substantially larger than the CO_2 emission from fossil fuel and industrial use in Australia in 2019 (~0.11 Pg C)(Friedlingstein et al., 2020). The eucalypt-dominated forests that burned in 2019 showed high resilience to fire and the rapid post-fire regrowth in most fire-affected forest areas, a process that was further enhanced by above-the-average precipitation in 2020. Such insights into forests are critical for improving Earth System Models to assess the net and compounded impacts of droughts, heatwaves, and forest fires on the terrestrial carbon fluxes and stocks (Sanderson and Fisher, 2020). The forest area in Australia is relatively small in comparison to the extensive areas of woodland, savanna, and grassland, but holds large carbon stocks (Keith et al., 2009) and is a carbon sink (Haverd et al., 2013a). 2019's record high temperatures, severe drought, and extensive forest fires serve as an early warning of the uncertain future of Australian forests over the coming decades because of projected climate change (Sanderson and Fisher, 2020). Changes in forest management, conservation, and supporting policies are needed to reduce forest vulnerability and enhance forest resilience to changes in climate, fire, and other disturbances while facilitating transitions that might be unavoidable.

CRediT authorship contribution statement

Yuanwei Qin: Conceptualization, Methodology, Software, Formal

analysis, Investigation, Writing – original draft. **Xiangming Xiao:** Conceptualization, Methodology, Formal analysis, Investigation, Writing – original draft. **Jean-Pierre Wigneron:** Methodology, Investigation, Writing – review & editing. **Philippe Ciais:** Methodology, Investigation, Writing – review & editing. **Josep G. Canadell:** Methodology, Investigation, Writing – review & editing. **Martin Brandt:** Investigation, Writing – review & editing. **Xiaojun Li:** Investigation, Writing – review & editing. **Lei Fan:** Investigation, Writing – review & editing. **Xiaocui Wu:** Software, Investigation, Writing – review & editing. **Hao Tang:** Investigation, Writing – review & editing. **Ralph Dubayah:** Investigation, Writing – review & editing. **Russell Doughty:** Software, Investigation, Writing – review & editing. **Sean Crowell:** Investigation, Writing – review & editing. **Bo Zheng:** Investigation, Writing – review & editing. **Berrien Moore:** Writing – review & editing.

Declaration of Competing Interest

The authors declare that they have no known competing financial interests or personal relationships that could have appeared to influence the work reported in this paper.

Acknowledgments

This study is supported in part by research grants from NASA Geostationary Carbon Cycle Observatory (GeoCarb) Mission (GeoCarb Contract # 80LARC17C0001), NSF (IIA-1946093), NASA Land Use and Land Cover Change program (NNX14AD78G) and NASA Science Team for the OCO Missions (80NSSC21K1077). JGC thanks the support from the Australian National Environmental Science Program-Climate Systems Hub. We thank the four reviewers for their time and effort in the review process and their comments and suggestions are invaluable for us to improve the manuscript.

Appendix A. Supplementary data

Supplementary data to this article can be found online at https://doi.org/10.1016/j.rse.2022.113087.

References

Abram, N.J., Henley, B.J., Sen Gupta, A., Lippmann, T.J.R., Clarke, H., Dowdy, A.J., Sharples, J.J., Nolan, R.H., Zhang, T., Wooster, M.J., Wurtzel, J.B., Meissner, K.J., Pitman, A.J., Ukkola, A.M., Murphy, B.P., Tapper, N.J., Boer, M.M., 2021. Connections of climate change and variability to large and extreme forest fires in southeast Australia. Commun. Earth Environ. 2, 1–17, 8.

Al-Yaari, A., Wigneron, J.-P., Dorigo, W., Colliander, A., Pellarin, T., Hahn, S., Mialon, A., Richaume, P., Fernandez-Moran, R., Fan, L., 2019. Assessment and inter-comparison of recently developed/reprocessed microwave satellite soil moisture products using ISMN ground-based measurements. Remote Sens. Environ. 224, 289–303.

Attiwill, P., 1992. Productivity of eucalyptus regnans forest regenerating after bushfire. South African Forestry J. 160, 1–6.

Avitabile, V., Herold, M., Heuvelink, G.B.M., Lewis, S.L., Phillips, O.L., Asner, G.P., Armston, J., Ashton, P.S., Banin, L., Bayol, N., Berry, N.J., Boeckx, P., Jong, B.H.J., DeVries, B., Girardin, C.A.J., Kearsley, E., Lindsell, J.A., Lopez-Gonzalez, G., Lucas, R., Malhi, Y., Morel, A., Mitchard, E.T.A., Nagy, L., Qie, L., Quinones, M.J., Ryan, C.M., Ferry, S.J.W., Sunderland, T., Laurin, G.V., Gatti, R.C., Valentini, R., Verbeeck, H., Wijaya, A., Willcock, S., 2016. An integrated pan-tropical biomass map using multiple reference datasets. Glob. Chang. Biol. 22, 1406–1420.

Baccini, A., Goetz, S.J., Walker, W.S., Laporte, N.T., Sun, M., Sulla-Menashe, D., Hackler, J., Beck, P.S.A., Dubayah, R., Friedl, M.A., Samanta, S., Houghton, R.A., 2012. Estimated carbon dioxide emissions from tropical deforestation improved by carbon-density maps. Nat. Clim. Chang. 2, 182–185.

Baccini, A., Walker, W., Carvalho, L., Farina, M., Sulla-Menashe, D., Houghton, R.A., 2017. Tropical forests are a net carbon source based on aboveground measurements of gain and loss. Science 358, 230–234.

Bacour, C., Maignan, F., MacBean, N., Porcar-Castell, A., Flexas, J., Frankenberg, C., Peylin, P., Chevallier, F., Vuichard, N., Bastrikov, V., 2019. Improving estimates of gross primary productivity by assimilating solar-induced fluorescence satellite retrievals in a terrestrial biosphere model using a process-based SIF model. J. Geophys. Res. Biogeosci. 124, 3281–3306.

Badgley, G., Field, C.B., Berry, J.A., 2017. Canopy near-infrared reflectance and terrestrial photosynthesis. Sci. Adv. 3, 1–5 e1602244.

Bastos, A., Friedlingstein, P., Sitch, S., Chen, C., Mialon, A., Wigneron, J.-P., Arora, V.K., Briggs, P.R., Canadell, J.G., Ciais, P., Chevallier, F., Cheng, L., Delire, C., Haverd, V., Jain, A.K., Joos, F., Kato, E., Lienert, S., Lombardozzi, D., Melton, J.R., Myneni, R., Nabel, J.E.M.S., Pongratz, J., Poulter, B., Ro¨denbeck, C., S´ef´erian, R., Tian, H., van Eck, C., Viovy, N., Vuichard, N., Walker, A.P., Wiltshire, A., Yang, J., Zaehle, S., Zeng, N., Zhu, D., 2018. Impact of the 2015/2016 El Nin˜o on the terrestrial carbon cycle constrained by bottom-up and top-down approaches. Philos. Trans. Roy. Soc. B: Biol. Sci 373, 1–11, 20170304.

Boer, M.M., Resco de Dios, V., Bradstock, R.A., 2020. Unprecedented burn area of Australian mega forest fires. Nat. Clim. Chang. 10, 171–172.

Bowman, D.M., Murphy, B.P., Boer, M.M., Bradstock, R.A., Cary, G.J., Cochrane, M.A., Fensham, R.J., Krawchuk, M.A., Price, O.F., Williams, R.J., 2013. Forest fire management, climate change, and the risk of catastrophic carbon losses. Front. Ecol. Environ. 11, 66–67.

Bowman, D., Williamson, G., Yebra, M., Lizundia-Loiola, J., Pettinari, M.L., Shah, S., Bradstock, R., Chuvieco, E., 2020. Wildfires: Australia needs national monitoring agency. Nature 584, 188–191.

Bowman, D.M.J.S., Williamson, G.J., Gibson, R.K., Bradstock, R.A., Keenan, R.J., 2021a. The severity and extent of the Australia 2019–20 Eucalyptus forest fires are not the legacy of forest management. Nat. Ecol. Evol. 5 (7), 1003–1010.

Bowman, D.M.J.S., Williamson, G.J., Price, O.F., Ndalila, M.N., Bradstock, R.A., 2021b. Australian forests, megafires and the risk of dwindling carbon stocks. Plant Cell Environ. 44, 347–355.

Brandt, M., Wigneron, J.-P., Chave, J., Tagesson, T., Penuelas, J., Ciais, P., Rasmussen, K., Tian, F., Mbow, C., Al-Yaari, A., 2018a. Satellite passive microwaves reveal recent climate-induced carbon losses in African drylands. Nat. Ecol. Evol. 2, 827.

Brandt, M., Wigneron, J.P., Chave, J., Tagesson, T., Penuelas, J., Ciais, P., Rasmussen, K., Tian, F., Mbow, C., Al-Yaari, A., Rodriguez-Fernandez, N., Schurgers, G., Zhang, W. M., Chang, J.F., Kerr, Y., Verger, A., Tucker, C., Mialon, A., Rasmussen, L.V., Fan, L., Fensholt, R., 2018b. Satellite passive microwaves reveal recent climate-induced carbon losses in African drylands. Nat. Ecol. Evol. 2, 827–835.

Bureau of Meteorology, 2020. Annual climate statement 2020. http://www.bom.gov.au/climate/current/annual/aus/. Bureau of Meteorology.

Byrne, B., Liu, J., Lee, M., Yin, Y., Bowman, K.W., Miyazaki, K., Norton, A.J., Joiner, J., Pollard, D.F., Griffith, D.W.T., Velazco, V.A., Deutscher, N.M., Jones, N.B., Paton-Walsh, C., 2021. The carbon cycle of southeast Australia during 2019–2020: drought, fires, and subsequent recovery. AGU Adv. *2* e2021AV000469.

Canadell, J.G., Meyer, C.P., Cook, G.D., Dowdy, A., Briggs, P.R., Knauer, J., Pepler, A., Haverd, V., 2021. Multi-decadal increase of forest burned area in Australia is linked to climate change. Nat. Commun. 12, 6921.

Carreiras, J.M.B., Quegan, S., Le Toan, T., Ho Tong Minh, D., Saatchi, S.S., Carvalhais, N., Reichstein, M., Scipal, K., 2017a. Coverage of high biomass forests by the ESA BIOMASS mission under defense restrictions. Remote Sens. Environ. 196, 154–162.

Carreiras, J.M.B., Shaun, Q.G., Toan, T.L., Minh, D.H.T., Saatchi, S.S., Carvalhais, N., Reichstein, M., Scipal, K., 2017b. Coverage of high biomass forests by the ESA BIOMASS mission under defense restrictions. Remote Sens. Environ. 196, 154–162.

Choat, B., Jansen, S., Brodribb, T.J., Cochard, H., Delzon, S., Bhaskar, R., Bucci, S.J., Feild, T.S., Gleason, S.M., Hacke, U.G., Jacobsen, A.L., Lens, F., Maherali, H., Martinez-Vilalta, J., Mayr, S., Mencuccini, M., Mitchell, P.J., Nardini, A., Pittermann, J., Pratt, R.B., Sperry, J.S., Westoby, M., Wright, I.J., Zanne, A.E., 2012. Global convergence in the vulnerability of forests to drought. Nature 491, 752–755.

Ciais, P., Reichstein, M., Viovy, N., Granier, A., Og´ee, J., Allard, V., Aubinet, M., Buchmann, N., Bernhofer, C., Carrara, A., Chevallier, F., De Noblet, N., Friend, A.D., Friedlingstein, P., Grünwald, T., Heinesch, B., Keronen, P., Knohl, A., Krinner, G., Loustau, D., Manca, G., Matteucci, G., Miglietta, F., Ourcival, J.M., Papale, D., Pilegaard, K., Rambal, S., Seufert, G., Soussana, J.F., Sanz, M.J., Schulze, E.D., Vesala, T., Valentini, R., 2005. Europe-wide reduction in primary productivity caused by the heat and drought in 2003. Nature 437, 529–533.

Clarke, P.J., Lawes, M.J., Murphy, B.P., Russell-Smith, J., Nano, C.E.M., Bradstock, R., Enright, N.J., Fontaine, J.B., Gosper, C.R., Radford, I., Midgley, J.J., Gunton, R.M., 2015. A synthesis of postfire recovery traits of woody plants in Australian ecosystems. Sci. Total Environ. 534, 31–42.

Collalti, A., Prentice, I.C., 2019. Is NPP proportional to GPP? Waring's hypothesis 20 years on. Tree Physiol. 39, 1473–1483.

Crisp, M.D., Burrows, G.E., Cook, L.G., Thornhill, A.H., Bowman, D.M.J.S., 2011. Flammable biomes dominated by eucalypts originated at the Cretaceous–Palaeogene boundary. Nat. Commun. 2, 193.

De Kauwe, M.G., Medlyn, B.E., Ukkola, A.M., Mu, M., Sabot, M.E.B., Pitman, A.J., Meir, P., Cernusak, L.A., Rifai, S.W., Choat, B., Tissue, D.T., Blackman, C.J., Li, X., Roderick, M., Briggs, P.R., 2020. Identifying areas at risk of drought-induced tree mortality across south-eastern Australia. Glob. Chang. Biol. 26, 5716–5733.

DISER, 2020. Estimating greenhouse gas emissions from bushfires in Australia's temperate forests: focus on 2019-20. Australian Government Department of Industry, Energy, Science, & Resources.

Doughty, R., Ko¨hler, P., Frankenberg, C., Magney, T.S., Xiao, X., Qin, Y., Wu, X., Moore, B., 2019. TROPOMI reveals dry-season increase of solar-induced chlorophyll fluorescence in the Amazon forest. Proc. Natl. Acad. Sci. 116, 22393–22398.

Dubayah, R., Blair, J.B., Goetz, S., Fatoyinbo, L., Hansen, M., Healey, S., Hofton, M., Hurtt, G., Kellner, J., Luthcke, S., Armston, J., Tang, H., Duncanson, L., Hancock, S., Jantz, P., Marselis, S., Patterson, P.L., Qi, W., Silva, C., 2020. The global ecosystem dynamics investigation: high-resolution laser ranging of the Earth's forests and topography. Sci. Remote Sens. 1, 100002.

Fan, L., Wigneron, J.P., Ciais, P., Chave, J., Brandt, M., Fensholt, R., Saatchi, S.S., Bastos, A., Al-Yaari, A., Hufkens, K., Qin, Y., Xiao, X., Chen, C., Myneni, R.B., Fernandez-Moran, R., Mialon, A., Rodriguez-Fernandez, N.J., Kerr, Y., Tian, F.,

Penuelas, J., 2019. Satellite-observed pantropical carbon dynamics. Nat. Plants 5, 944–951.
Fernandez-Moran, R., Al-Yaari, A., Mialon, A., Mahmoodi, A., Al Bitar, A., De Lannoy, G., Rodriguez-Fernandez, N., Lopez-Baeza, E., Kerr, Y., Wigneron, J.P., 2017. SMOS-IC: an alternative SMOS soil moisture and vegetation optical depth product. Remote Sens. 9, 457.
Frankenberg, C., Fisher, J.B., Worden, J., Badgley, G., Saatchi, S.S., Lee, J.-E., Toon, G.C., Butz, A., Jung, M., Kuze, A., Yokota, T., 2011. New global observations of the terrestrial carbon cycle from GOSAT: patterns of plant fluorescence with gross primary productivity. Geophys. Res. Lett. 38.
Frappart, F., Wigneron, J.-P., Li, X., Liu, X., Al-Yaari, A., Fan, L., Wang, M., Moisy, C., Le Masson, E., Aoulad Lafkih, Z., Vall´e, C., Ygorra, B., Baghdadi, N., 2020. Global monitoring of the vegetation dynamics from the vegetation optical depth (VOD): a review. Remote Sens. 12, 2915.
Friedlingstein, P., O'Sullivan, M., Jones, M.W., Andrew, R.M., Hauck, J., Olsen, A., Peters, G.P., Peters, W., Pongratz, J., Sitch, S., Le Qu´er´e, C., Canadell, J.G., Ciais, P., Jackson, R.B., Alin, S., Aragа˜o, L.E.O.C., Arneth, A., Arora, V., Bates, N.R., Becker, M., Benoit-Cattin, A., Bittig, H.C., Bopp, L., Bultan, S., Chandra, N., Chevallier, F., Chini, L.P., Evans, W., Florentie, L., Forster, P.M., Gasser, T., Gehlen, M., Gilfillan, D., Gkritzalis, T., Gregor, L., Gruber, N., Harris, I., Hartung, K., Haverd, V., Houghton, R.A., Ilyina, T., Jain, A.K., Joetzjer, E., Kadono, K., Kato, E., Kitidis, V., Korsbakken, J.I., Landschützer, P., Lef`evre, N., Lenton, A., Lienert, S., Liu, Z., Lombardozzi, D., Marland, G., Metzl, N., Munro, D.R., Nabel, J.E.M.S., Nakaoka, S.I., Niwa, Y., O'Brien, K., Ono, T., Palmer, P.I., Pierrot, D., Poulter, B., Resplandy, L., Robertson, E., Ro¨denbeck, C., Schwinger, J., S´ef´erian, R., Skjelvan, I., Smith, A.J.P., Sutton, A.J., Tanhua, T., Tans, P.P., Tian, H., Tilbrook, B., van der Werf, G., Vuichard, N., Walker, A.P., Wanninkhof, R., Watson, A.J., Willis, D., Wiltshire, A.J., Yuan, W., Yue, X., Zaehle, S., 2020. Global carbon budget 2020. Earth Syst. Sci. Data 12, 3269–3340.
Fu, Z., Li, D., Hararuk, O., Schwalm, C., Luo, Y., Yan, L., Niu, S., 2017. Recovery time and state change of terrestrial carbon cycle after disturbance. Environ. Res. Lett. 12, 104004.
Giglio, L., Justice, C., 2015. MOD14A2 MODIS/terra thermal anomalies/fire 8-day L3 global 1km SIN grid V006 [data set]. In: N.E.L. DAAC. (Ed.).
Guanter, L., Aben, I., Tol, P., Krijger, J.M., Hollstein, A., Kohler, P., Damm, A., Joiner, J., Frankenberg, C., Landgraf, J., 2015. Potential of the TROPOspheric monitoring instrument (TROPOMI) onboard the Sentinel-5 precursor for the monitoring of terrestrial chlorophyll fluorescence. Atmos. Measur. Techniques 8, 1337–1352.
Hamdan, O., Khali Aziz, H., Mohd Hasmadi, I., 2014. L-band ALOS PALSAR for biomass estimation of Matang mangroves, Malaysia. Remote Sens. Environ. 155, 69–78.
Hansen, M.C., Potapov, P., Tyukavina, A., 2019. Comment on "tropical forests are a net carbon source based on aboveground measurements of gain and loss". Science 363, eaar3629.
Harris, N.L., 2012. Baseline map of carbon emissions from deforestation in tropical regions. Science 336, 1573–1576.
Harris, N.L., Gibbs, D.A., Baccini, A., Birdsey, R.A., de Bruin, S., Farina, M., Fatoyinbo, L., Hansen, M.C., Herold, M., Houghton, R.A., Potapov, P.V., Suarez, D.R., Roman-Cuesta, R.M., Saatchi, S.S., Slay, C.M., Turubanova, S.A., Tyukavina, A., 2021. Global maps of twenty-first century forest carbon fluxes. Nat. Clim. Chang. 11 (3), 234–240.
Haverd, V., Raupach, M.R., Briggs, P.R., Canadell, J.G., Davis, S.J., Law, R.M., Meyer, C. P., Peters, G.P., Pickett-Heaps, C., Sherman, B., 2013a. The Australian terrestrial carbon budget. Biogeosciences 10, 851–869.
Haverd, V., Raupach, M.R., Briggs, P.R., Canadell, J.G., Isaac, P., Pickett-Heaps, C., Roxburgh, S.H., van Gorsel, E., Viscarra Rossel, R.A., Wang, Z., 2013b. Multiple observation types reduce uncertainty in Australia's terrestrial carbon and water cycles. Biogeosciences 10, 2011–2040.
Hubau, W., Lewis, S.L., Phillips, O.L., Affum-Baffoe, K., Beeckman, H., Cuní-Sanchez, A., Daniels, A.K., Ewango, C.E.N., Fauset, S., Mukinzi, J.M., Sheil, D., Sonk´e, B., Sullivan, M.J.P., Sunderland, T.C.H., Taedoumg, H., Thomas, S.C., White, L.J.T., Abernethy, K.A., Adu-Bredu, S., Amani, C.A., Baker, T.R., Banin, L.F., Baya, F., Begne, S.K., Bennett, A.C., Benedet, F., Bitariho, R., Bocko, Y.E., Boeckx, P., Boundja, P., Brienen, R.J.W., Brncic, T., Chezeaux, E., Chuyong, G.B., Clark, C.J., Collins, M., Comiskey, J.A., Coomes, D.A., Dargie, G.C., de Haulleville, T., Kamdem, M.N.D., Doucet, J.-L., Esquivel-Muelbert, A., Feldpausch, T.R., Fofanah, A., Foli, E.G., Gilpin, M., Gloor, E., Gonmadje, C., Gourlet-Fleury, S., Hall, J.S., Hamilton, A.C., Harris, D.J., Hart, T.B., Hockemba, M.B.N., Hladik, A., Ifo, S.A., Jeffery, K.J., Jucker, T., Yakusu, E.K., Kearsley, E., Kenfack, D., Koch, A., Leal, M.E., Levesley, A., Lindsell, J.A., Lisingo, J., Lopez-Gonzalez, G., Lovett, J.C., Makana, J.-R., Malhi, Y., Marshall, A.R., Martin, J., Martin, E.H., Mbayu, F.M., Medjibe, V.P., Mihindou, V., Mitchard, E.T.A., Moore, S., Munishi, P.K.T., Bengone, N.N., Ojo, L., Ondo, F.E., Peh, K.S.H., Pickavance, G.C., Poulsen, A.D., Poulsen, J.R., Qie, L., Reitsma, J., Rovero, F., Swaine, M.D., Talbot, J., Taplin, J., Taylor, D.M., Thomas, D.W., Toirambe, B., Mukendi, J.T., Tuagben, D., Umunay, P. M., van der Heijden, G.M.F., Verbeeck, H., Vleminckx, J., Willcock, S., Wo¨ll, H., Woods, J.T., Zemagho, L., 2020. Asynchronous carbon sink saturation in African and Amazonian tropical forests. Nature 579, 80–87.
Huete, A.R., Liu, H.Q., Batchily, K., van Leeuwen, W., 1997. A comparison of vegetation indices over a global set of TM images for EOS-MODIS. Remote Sens. Environ. 59, 440–451.
Huete, A., Didan, K., Miura, T., Rodriguez, E.P., Gao, X., Ferreira, L.G., 2002. Overview of the radiometric and biophysical performance of the MODIS vegetation indices. Remote Sens. Environ. 83, 195–213.
Huffman, G.J., Stocker, E.F., Bolvin, D.T., Nelkin, E.J., Tan, J., 2019. GPM IMERG Final Precipitation L3 1 month 0.1 degree x 0.1 degree V06, Greenbelt, MD. In: Goddard Earth Sciences Data and Information Services Center (GES DISC).
Jackson, T., Schmugge, T., 1991. Vegetation effects on the microwave emission of soils. Remote Sens. Environ. 36, 203–212.
Keith, H., Mackey, B.G., Lindenmayer, D.B., 2009. Re-evaluation of forest biomass carbon stocks and lessons from the world's most carbon-dense forests. Proc. Natl. Acad. Sci. U. S. A. 106, 11635–11640.
Keith, H., Mackey, B., Berry, S., Lindenmayer, D., Gibbons, P., 2010. Estimating carbon carrying capacity in natural forest ecosystems across heterogeneous landscapes: addressing sources of error. Glob. Chang. Biol. 16, 2971–2989.
Keith, H., Lindenmayer, D.B., Mackey, B.G., Blair, D., Carter, L., McBurney, L., Okada, S., Konishi-Nagano, T., 2014. Accounting for biomass carbon stock change due to wildfire in temperate forest landscapes in Australia. PLoS One 9.
King, A.D., Pitman, A.J., Henley, B.J., Ukkola, A.M., Brown, J.R., 2020. The role of climate variability in Australian drought. Nat. Clim. Chang. 10, 177–179.
Kohler, P., Frankenberg, C., Magney, T.S., Guanter, L., Joiner, J., Landgraf, J., 2018. Global retrievals of solar-induced chlorophyll fluorescence with TROPOMI: first results and Intersensor comparison to OCO-2. Geophys. Res. Lett. 45, 10456–10463.
Konings, A.G., Gentine, P., 2017. Global variations in ecosystem-scale isohydricity. Glob. Chang. Biol. 23, 891–905.
Li, X., Al-Yaari, A., Schwank, M., Fan, L., Frappart, F., Swenson, J., Wigneron, J.P., 2020a. Compared performances of SMOS-IC soil moisture and vegetation optical depth retrievals based on Tau-Omega and Two-Stream microwave emission models. Remote Sens. Environ. 236, 111502.
Li, X.J., Wigneron, J.-P., Fan, L., Frappart, F., Yueh, S., Colliander, A., Ebtehaj, A., Gao, L., Fernandez-Moran, R., Liu, X.Z., Wang, M.J., Ma, H.L., Moisy, C., Ciais, P., 2022. A new SMAP soil moisture and vegetation optical depth product (SMAP-IB): Algorithm, assessment and inter-comparison. Remote Sens. Environ. 271, 1–21, 112921.
Li, X., Wigneron, J.-P., Frappart, F., Fan, L., Ciais, P., Fensholt, R., Entekhabi, D., Brandt, M., Konings, A.G., Liu, X., Wang, M., Al-Yaari, A., Moisy, C., 2020b. Global-scale assessment and inter-comparison of recently developed/reprocessed microwave satellite vegetation optical depth products. Remote Sens. Environ. 112208.
Li, F., Zhang, X., Kondragunta, S., 2021. Highly anomalous fire emissions from the 2019–2020 Australian bushfires. Environ. Res. 3, 1–20, 105005, (Communications).
Liu, Y.Y., de Jeu, R.A.M., McCabe, M.F., Evans, J.P., van Dijk, A.I.J.M., 2011. Global long-term passive microwave satellite-based retrievals of vegetation optical depth. Geophys. Res. Lett. 38, 1–6. L18402.
Liu, Y.Y., van Dijk, A.I.J.M., de Jeu, R.A.M., Canadell, J.G., McCabe, M.F., Evans, J.P., Wang, G.J., 2015. Recent reversal in loss of global terrestrial biomass. Nat. Clim. Chang. 5, 470–474.
Lucas, R., Armston, J., Fairfax, R., Fensham, R., Accad, A., Carreiras, J., Kelley, J., Bunting, P., Clewley, D., Bray, S., Metcalfe, D., Dwyer, J., Bowen, M., Eyre, T., Laidlaw, M., Shimada, M., 2010. An evaluation of the ALOS PALSAR L-band backscatter—above ground biomass relationship Queensland, Australia: impacts of surface moisture condition and vegetation structure. Ieee J. Select. Top. Appl. Earth Observ. Remote Sens. 3, 576–593.
Ma, J., Xiao, X.M., Qin, Y.W., Chen, B.Q., Hu, Y.M., Li, X.P., Zhao, B., 2017. Estimating aboveground biomass of broadleaf, needleleaf, and mixed forests in northeastern China through analysis of 25-m ALOS/PALSAR mosaic data. For. Ecol. Manag. 389, 199–210.
Myneni, R., Knyazikhin, Y., Park, T., 2015. MCD15A3H MODIS/Terra+aqua leaf area index/FPAR 4-day L4 Global 500m SIN Grid V006. In: N.E.L.P. DAAC (Ed.).
Nolan, R.H., Boer, M.M., Collins, L., de Dios, V.R., Clarke, H., Jenkins, M., Kenny, B., Bradstock, R.A., 2020. Causes and consequences of eastern Australia's 2019-20 season of mega-fires. Glob. Chang. Biol. 26, 1039–1041.
Paul, K.I., Roxburgh, S.H., Chave, J., England, J.R., Zerihun, A., Specht, A., Lewis, T., Bennett, L.T., Baker, T.G., Adams, M.A., Huxtable, D., Montagu, K.D., Falster, D.S., Feller, M., Sochacki, S., Ritson, P., Bastin, G., Bartle, J., Wildy, D., Hobbs, T., Larmour, J., Waterworth, R., Stewart, H.T.L., Jonson, J., Forrester, D.I., Applegate, G., Mendham, D., Bradford, M., O'Grady, A., Green, D., Sudmeyer, R., Rance, S.J., Turner, J., Barton, C., Wenk, E.H., Grove, T., Attiwill, P.M., Pinkard, E., Butler, D., Brooksbank, K., Spencer, B., Snowdon, P., O'Brien, N., Battaglia, M., Cameron, D.M., Hamilton, S., McAuthur, G., Sinclair, J., 2016. Testing the generality of above-ground biomass allometry across plant functional types at the continent scale. Glob. Chang. Biol. 22, 2106–2124.
Qin, Y.W., Xiao, X.M., Dong, J.W., Zhang, G.L., Shimada, M., Liu, J.Y., Li, C.G., Kou, W. L., Moore, B., 2015. Forest cover maps of China in 2010 from multiple approaches and data sources: PALSAR, Landsat, MODIS, FRA, and NFI. ISPRS J. Photogramm. Remote Sens. 109, 1–16.
Qin, Y.W., Xiao, X.M., Dong, J.W., Zhang, G.L., Roy, P.S., Joshi, P.K., Gilani, H., Murthy, M.S.R., Jin, C., Wang, J., Zhang, Y., Chen, B.Q., Menarguez, M.A., Biradar, C.M., Bajgain, R., Li, X.P., Dai, S.Q., Hou, Y., Xin, F.F., Moore, B., 2016. Mapping forests in monsoon Asia with ALOS PALSAR 50-m mosaic images and MODIS imagery in 2010. Sci. Rep. 6.
Qin, Y.W., Xiao, X.M., Dong, J.W., Zhou, Y.T., Wang, J., Doughty, R.B., Chen, Y., Zou, Z. H., Moore, B., 2017. Annual dynamics of forest areas in South America during 2007-2010 at 50m spatial resolution. Remote Sens. Environ. 201, 73–87.
Qin, Y.W., Xiao, X.M., Dong, J.W., Zhang, Y., Wu, X.C., Shimabukuro, Y., Arai, E., Biradar, C., Wang, J., Zou, Z.H., Liu, F., Shi, Z., Doughty, R., Moore, B., 2019. Improved estimates of forest cover and loss in the Brazilian Amazon in 2000-2017. Nat. Sustain. 2, 764–772.
Qin, Y., Xiao, X., Wigneron, J.-P., Ciais, P., Canadell, J.G., Brandt, M., Li, X., Fan, L., Wu, X., Tang, H., Dubayah, R., Doughty, R., Chang, Q., Crowell, S., Zheng, B., Neal, K., Celis, J.A., Moore, B., 2021a. Annual maps of forests in Australia from analyses of microwave and optical images with FAO Forest definition. J. Remote Sens. 9784657, 2021.

Qin, Y.W., Xiao, X.M., Wigneron, J.P., Ciais, P., Brandt, M., Fan, L., Li, X.J., Crowell, S., Wu, X.C., Doughty, R., Zhang, Y., Liu, F., Sitch, S., Moore, B., 2021b. Carbon loss from forest degradation exceeds that from deforestation in the Brazilian Amazon. Nat. Clim. Chang. 11, 442–448.
Rodríguez-Fern´andez, N.J., Mialon, A., Mermoz, S., Bouvet, A., Richaume, P., Al Bitar, A., Al-Yaari, A., Brandt, M., Kaminski, T., Le Toan, T., 2018. An evaluation of SMOS L-band vegetation optical depth (L-VOD) data sets: high sensitivity of L-VOD to above-ground biomass in Africa. Biogeosciences 15, 4627–4645.
Rodriguez-Fernandez, N.J., Mialon, A., Mermoz, S., Bouyet, A., Richaume, P., Al Bitar, A., Al-Yaari, A., Brandt, M., Kaminski, T., Toan, T.L., Kerr, Y.H., Wigneron, J. P., 2018. An evaluation of SMOS L-band vegetation optical depth (L-VOD) data sets: high sensitivity of L-VOD to above-ground biomass in Africa. Biogeosciences 15, 4627–4645.
Roxburgh, S.H., Barrett, D.J., Berry, S.L., Carter, J.O., Davies, I.D., Gifford, R.M., Kirschbaum, M.U.F., McBeth, B.P., Noble, I.R., Parton, W.G., Raupach, M.R., Roderick, M.L., 2004. A critical overview of model estimates of net primary productivity for the Australian continent. Funct. Plant Biol. 31, 1043–1059.
Ryan, M.G., Binkley, D., Fownes, J.H., Giardina, C.P., Senock, R.S., 2004. An experimental test of the causes of forest growth decline with stand age. Ecol. Monogr. 74, 393–414.
Saatchi, S.S., Harris, N.L., Brown, S., Lefsky, M., Mitchard, E.T.A., Salas, W., Zutta, B.R., Buermann, W., Lewis, S.L., Hagen, S., Petrova, S., White, L., Silman, M., Morel, A., 2011. Benchmark map of forest carbon stocks in tropical regions across three continents. Proc. Natl. Acad. Sci. U. S. A. 108, 9899–9904.
Sanderson, B.M., Fisher, R.A., 2020. A fiery wake-up call for climate science. Nat. Clim. Chang. 10, 175–177.
Santoro, M., Quegan, S., 2019. CCI Biomass Product User Guide. ESA Climate Change Initiative.
Schwalm, C.R., Anderegg, W.R.L., Michalak, A.M., Fisher, J.B., Biondi, F., Koch, G., Litvak, M., Ogle, K., Shaw, J.D., Wolf, A., Huntzinger, D.N., Schaefer, K., Cook, R., Wei, Y., Fang, Y., Hayes, D., Huang, M., Jain, A., Tian, H., 2017. Global patterns of drought recovery. Nature 548, 202–205.
Seidl, R., Thom, D., Kautz, M., Martin-Benito, D., Peltoniemi, M., Vacchiano, G., Wild, J., Ascoli, D., Petr, M., Honkaniemi, J., Lexer, M.J., Trotsiuk, V., Mairota, P., Svoboda, M., Fabrika, M., Nagel, T.A., Reyer, C.P.O., 2017. Forest disturbances under climate change. Nat. Clim. Chang. 7, 395–402.
Shimada, M., Itoh, T., Motooka, T., Watanabe, M., Shiraishi, T., Thapa, R., Lucas, R., 2014. New global forest/non-forest maps from ALOS PALSAR data (2007-2010). Remote Sens. Environ. 155, 13–31.
Shiraishi, T., Hirata, R., 2021. Estimation of carbon dioxide emissions from the megafires of Australia in 2019–2020. Sci. Rep. 11, 8267.
The Biomass Plot Library, 2022. The Biomass Plot Library. http://data.auscover.org.au/xwiki/bin/view/Product+pages/Biomass+Plot+Library#HReferences.
Tian, F., Wigneron, J.-P., Ciais, P., Chave, J., Og´ee, J., Pen˜uelas, J., Ræbild, A., Domec, J.-C., Tong, X., Brandt, M., 2018. Coupling of ecosystem-scale plant water storage and leaf phenology observed by satellite. Nat. Ecol. Evol. 2 (9), 1428–1435.
Tucker, C.J., 1979. Red and photographic infrared linear combinations for monitoring vegetation. Remote Sens. Environ. 8, 127–150.
Turner, A.J., Ko¨hler, P., Magney, T.S., Frankenberg, C., Fung, I., Cohen, R.C., 2020. A double peak in the seasonality of California's photosynthesis as observed from space. Biogeosciences 17, 405–422.
van der Velde, I.R., van der Werf, G.R., Houweling, S., Maasakkers, J.D., Borsdorff, T., Landgraf, J., Tol, P., van Kempen, T.A., van Hees, R., Hoogeveen, R., Veefkind, J.P., Aben, I., 2021. Vast CO2 release from Australian fires in 2019–2020 constrained by satellite. Nature 597, 366–369.
Volkova, L., Roxburgh, S.H., Weston, C.J., Benyon, R.G., Sullivan, A.L., Polglase, P.J., 2018. Importance of disturbance history on net primary productivity in the world's most productive forests and implications for the global carbon cycle. Glob. Chang. Biol. 24, 4293–4303.
Wan, Z., Hook, S., Hulley, G., 2015. MOD11A1 MODIS/Terra Land Surface Temperature/Emissivity Daily L3 Global 1km SIN Grid V006 [Data set]. In: N.E.L.P. DAAC. (Ed.).
Wigneron, J.-P., Jackson, T., O'neill, P., De Lannoy, G., De Rosnay, P., Walker, J., Ferrazzoli, P., Mironov, V., Bircher, S., Grant, J., 2017a. Modelling the passive microwave signature from land surfaces: a review of recent results and application to the L-band SMOS & SMAP soil moisture retrieval algorithms. Remote Sens. Environ. 192, 238–262.
Wigneron, J.P., Jackson, T.J., O'Neill, P., De Lannoy, G., de Rosnay, P., Walker, J.P., Ferrazzoli, P., Mironov, V., Bircher, S., Grant, J.P., Kurum, M., Schwank, M., Munoz-Sabater, J., Das, N., Royer, A., Al-Yaari, A., Al Bitar, A., Fernandez-Moran, R., Lawrence, H., Mialon, A., Parrens, M., Richaume, P., Delwart, S., Kerr, Y., 2017b. Modelling the passive microwave signature from land surfaces: a review of recent results and application to the L-band SMOS & SMAP soil moisture retrieval algorithms. Remote Sens. Environ. 192, 238–262.
Wigneron, J.-P., Fan, L., Ciais, P., Bastos, A., Brandt, M., Chave, J., Saatchi, S., Baccini, A., Fensholt, R., 2020. Tropical forests did not recover from the strong 2015–2016 El Nin˜o event. *Science*. Advances 6, eaay4603.
Xiao, X., Boles, S., Frolking, S., Salas, W., Moore, B., Li, C., He, L., Zhao, R., 2002. Observation of flooding and rice transplanting of paddy rice fields at the site to landscape scales in China using VEGETATION sensor data. Int. J. Remote Sens. 23, 3009–3022.
Xiao, X.M., Hollinger, D., Aber, J., Goltz, M., Davidson, E.A., Zhang, Q.Y., Moore, B., 2004a. Satellite-based modeling of gross primary production in an evergreen needleleaf forest. Remote Sens. Environ. 89, 519–534.
Xiao, X.M., Zhang, Q.Y., Braswell, B., Urbanski, S., Boles, S., Wofsy, S., Berrien, M., Ojima, D., 2004b. Modeling gross primary production of temperate deciduous broadleaf forest using satellite images and climate data. Remote Sens. Environ. 91, 256–270.
Xiao, X.M., Boles, S., Liu, J.Y., Zhuang, D.F., Frolking, S., Li, C.S., Salas, W., Moore, B., 2005. Mapping paddy rice agriculture in southern China using multi-temporal MODIS images. Remote Sens. Environ. 95, 480–492.
Wigneron, J.-P., Li, X.J., Frappart, F., Fan, L., Al-Yaari, A., Lannoy, G., Liu, X.Z., Wang, M.J., Masson, E., Moisy, C., 2021. SMOS-IC data record of soil moisture and L-VOD: Historical development, applications and perspectives. Remote Sens. Environ. 254, 1–20, 112238.
Xiao, X.M., Boles, S., Frolking, S., Li, C.S., Babu, J.Y., Salas, W., Moore, B., 2006. Mapping paddy rice agriculture in south and Southeast Asia using multi-temporal MODIS images. Remote Sens. Environ. 100, 95–113.
Xu, L., Saatchi, S.S., Yang, Y., Yu, Y., Pongratz, J., Bloom, A.A., Bowman, K., Worden, J., Liu, J., Yin, Y., Domke, G., McRoberts, R.E., Woodall, C., Nabuurs, G.-J., de Miguel, S., Keller, M., Harris, N., Maxwell, S., Schimel, D., 2021. Changes in global terrestrial live biomass over the 21st century. Sci. Adv. 7, eabe9829.
Yang, Y., Saatchi, S.S., Xu, L., Yu, Y., Choi, S., Phillips, N., Kennedy, R., Keller, M., Knyazikhin, Y., Myneni, R.B., 2018. Post-drought decline of the Amazon carbon sink. Nat. Commun. 9, 3172.
Yin, Y., Byrne, B., Liu, J., Wennberg, P.O., Davis, K.J., Magney, T., Ko¨hler, P., He, L., Jeyaram, R., Humphrey, V., Gerken, T., Feng, S., Digangi, J.P., Frankenberg, C., 2020. Cropland carbon uptake delayed and reduced by 2019 Midwest floods. AGU Adv. 1 e2019AV000140.
Zhang, Y., Xiao, X., Wu, X., Zhou, S., Zhang, G., Qin, Y., Dong, J., 2017a. A global moderate resolution dataset of gross primary production of vegetation for 2000–2016. Sci. Data 4, 170165.
Zhang, Y., Xiao, X., Wu, X., Zhou, S., Zhang, G., Qin, Y., Dong, J., 2017b. A global moderate resolution dataset of gross primary production of vegetation for 2000–2016. Sci. Data 4, 170165.